

**LARGE SCALE WIND TUNNEL HUMIDITY SENSOR USING LASER DIODE
ABSORPTION SPECTROSCOPY**

By

William Timothy Mallory Jr.

Thesis

Submitted to the Faculty of the
Graduate School of Vanderbilt University
in partial fulfillment of the requirements
for the degree of

MASTER OF SCIENCE

in

Mechanical Engineering

August 11, 2017

Nashville, Tennessee

Approved:

Robert W. Pitz, Ph.D.

Greg D. Walker, Ph.D.

David H. Plemmons, Ph.D.

Joseph A. Wehrmeyer, Ph.D.

DEDICATION

I dedicate this thesis to Amanda and Mason. Your love, support and understanding throughout this process is appreciated more than you will ever know. I couldn't have made it to the finish line without you.

Mason, anything you set your mind to is achievable through hard work, dedication and determination.

ACKNOWLEDGEMENTS

I want to thank my committee members for all of their guidance, support and time they have graciously provided me throughout this process. A special thanks to Dr. David Plemmons for the countless hours of patient explanation and support you have given me. I am sincerely grateful.

I also want to acknowledge the Air Force's Palace Acquire Program for giving me the opportunity to pursue my graduate degree and Arnold Engineering Development Complex for allowing me to conduct my research at such a unique, world-class facility. Thanks to my supervisors for their support and commitment to my continued education.

TABLE OF CONTENTS

	Page
DEDICATION	ii
ACKNOWLEDGEMENTS	iii
LIST OF TABLES	vi
LIST OF FIGURES	vii
Chapter	
I. Introduction	1
Summary	1
Motivation	3
Background	5
II. Theory	10
Laser Diode Absorption	10
Line Shape Function Approximation	15
Final Computational Equation.....	16
III. Spectral Model and Curve Fitting Tool.....	19
Spectral Model	19
Absorption Line Selection.....	21
Curve Fitting Tool	27
IV. Experimental Setup	34
Absorption Cell Setup	34
Sensor Calibration Setup.....	36
Wind Tunnel System Setup.....	37
V. Experimental Results and Discussion	39
Absorption Cell Results.....	39
Sensor Calibration Results	43
Wind Tunnel System Results	52

VI. Conclusion.....	55
Summary of Research and Results.....	55
Future Plans and Recommendations	57
REFERENCES	58

LIST OF TABLES

Table	Page
Table I: Variables list for Equation 16.....	18
Table II: HITRAN parameters for the 1394.7 nm and 1395.0 nm absorption lines	27
Table III: Etalon constants for the 1394.7 nm and 1395.0 nm absorption lines	31
Table IV: Error component and total uncertainty values for PMEL calibration	51

LIST OF FIGURES

Figure	Page
Figure 1: CMH illustration.....	2
Figure 2: Beer-Lambert Law illustration	10
Figure 3: Absorption Model GUI	19
Figure 4: Absorption spectrum for H ₂ O between 1391 nm and 1397 nm at T=300 K, P=14.7 PSI, X _{H₂O} =0.002412 and L=16.0 ft	23
Figure 5: Absorption spectrum for feature 1 at T=300 K, P=14.7 PSI, X _{H₂O} =0.002412 and L=16.0 ft	24
Figure 6: Features 10 and 11, 1394.7 nm and 1395.0 nm respectively, for three different conditions. (a) T=300 K, P=14.7 PSI, X _{H₂O} =0.002412 and L=16.0 ft, (b) T=300 K, P=0.5 PSI, X _{H₂O} =0.0001 and L=16.0 ft and (c) T=300 K, P=27 PSI, X _{H₂O} =0.01 and L=16.0 ft...	26
Figure 7: Curve Fitting Tool for raw absorption data.....	28
Figure 8: Curve Fitting Tool for raw absorption data showing raw data.....	29
Figure 9: Example raw etalon signal	30
Figure 10: Curve Fitting Tool result for 1395.0 nm data set	33
Figure 11: Absorption Cell setup.....	34
Figure 12: PMEL calibration setup.....	37
Figure 13: LH System setup	38
Figure 14: Mole fraction data for the Vaisala hand-held meter (2 channels) and LH for the 1394.7 nm absorption line.....	39
Figure 15: Vaisala/LH comparison for the Vaisala hand-held measurements for the 1394.7 nm absorption line.....	40
Figure 16: Mole fraction data for the LH and CMH for the 1394.7 nm absorption line	41
Figure 17: CMH/LH comparison for the 1394.7 nm absorption line	42
Figure 18: Mole fraction data for the LH and HG for two absorption lines (a) 1394.7 nm and (b) 1395.0 nm	44

Figure 19: Log-Log plot of LH vs. HG for the two absorption lines (a) 1394.7 nm and (b) 1395.0 nm	46
Figure 20: LH/HG vs. HG for (a) 1394.7 nm and (b) 1395.0 nm.....	48
Figure 21: Log-Log plot of Calibrated LH vs. HG for the two absorption lines (a) 1394.7 nm and (b) 1395.0 nm.....	50
Figure 22: 4T mole fraction data for Averaged CMH and Calibrated LH	53
Figure 23: Calibrated LH vs. Averaged CMH mole fraction measurements	54

CHAPTER I

INTRODUCTION

Summary

Laser diode absorption (LDA) spectroscopy, also referred to as tunable-diode laser absorption spectroscopy (TDLAS), is a powerful non-intrusive diagnostic technique used to measure flow properties in extreme environments experienced in aerospace ground testing. For over three decades, LDA has been successfully implemented in a wide variety of applications including: flat flame and slot burner combustion measurements [1] [2], water vapor monitoring in shock tubes [3] [4], scramjet combustion measurements [5] [6], microgravity combustion measurements [7], pulse detonation engine combustion measurements [8], subsonic mass flux measurements [9], supersonic mass flux measurements [10] [11] [12], and many others unrelated to ground testing that are not mentioned here.

A cornerstone for the success and utility of LDA spectroscopy is the continuous evolution of the diode laser which has been driven primarily by the telecommunications industry and its desire for single mode laser beams and fiber optic beam delivery. From the early Pb-salt type diode lasers to the more modern InGaAsP diode lasers and quantum cascade lasers (QCL), their wavelength stability and tunability has increased significantly and resolution has improved leading to the measurement of more refined line shape parameters and thus a more accurate measurement capability while decreasing in cost. Combining these enhancements with the capability of these lasers to operate at room temperatures and to deliver their signal through fiber

optics, has sparked a plethora of interest into developing practical uses for these types of systems.

Ground test facility humidity monitoring is of great interest and the subject of the work herein. The current technique that is widely used to make this type of measurement is a chilled mirror or dew point hygrometer (CMH). This type of system operates based on the illustration shown in Figure 1.

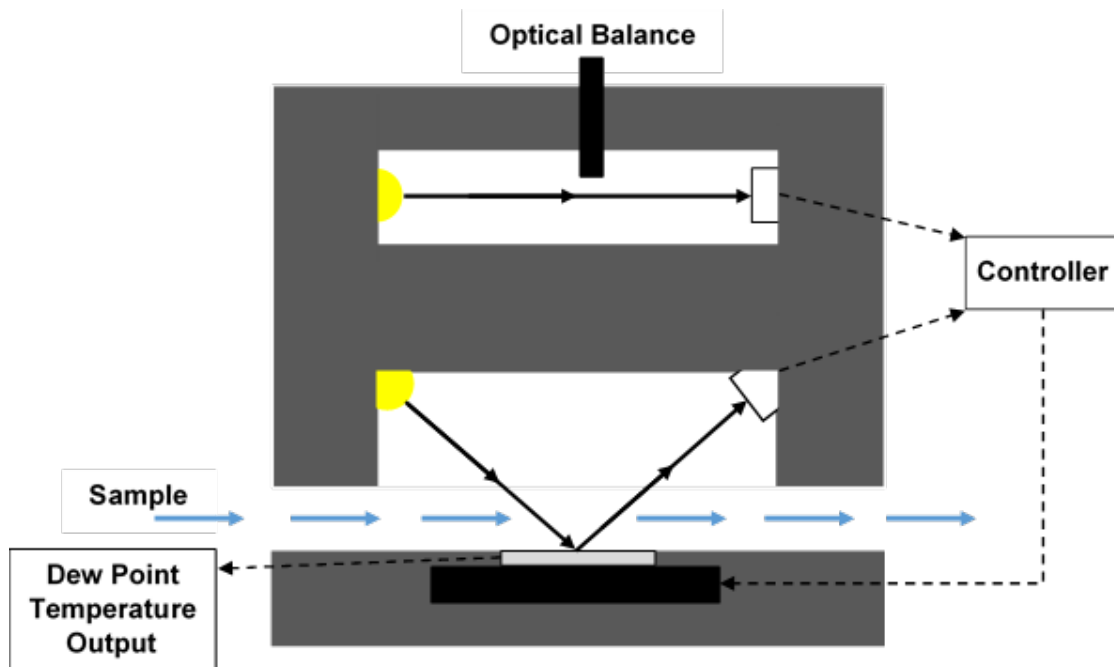


Figure 1: CMH illustration

A gas sample is directed through the system and across a temperature controlled mirror. The temperature of the mirror is lowered until a thin layer of condensation forms on its surface. Once the temperature and condensation layer reach equilibrium, a thermometer embedded in the mirror measures the dew point temperature. The existence of condensation on the mirror is detected by a decrease in light intensity reflected off the mirror from a light source into a photodetector. An optical balance is used to balance the incident light intensity once

contamination on the mirror is present which decreases the incident optical intensity [13]. While this measurement technique is considered state-of-the-art in terms of accuracy, there are several challenges with using this type of system to measure humidity level in ground test facility flows. Thus, the idea of supplementing or replacing a CMH with a diode laser based humidity measuring device is becoming more and more appealing.

The purpose of this study is to investigate the feasibility of using a laser based humidity measurement technique to more efficiently and effectively measure the humidity flow condition in a ground test facility. This will be achieved through the development of a spectral model, to determine the best spectral line(s) for the particular set of conditions experienced in the facility, and analysis algorithms to determine the flow humidity. The algorithms will then be verified through laboratory experiments and facility flow data and also validated through data from a National Institute of Standards and Technology (NIST) traceable humidity generator (HG).

Motivation

Humidity is an extremely important facility parameter in AEDC's 4T, 16T and 16S wind tunnels due to its effect on the calculated Mach (M) and Reynolds (Re) numbers which are primary facility parameters that are set for each test point and reported to the test customer. At certain conditions in the operational envelope of these facilities, if the level of humidity is high enough water will begin to condense and form fog in the test section. When this happens, the physical properties of the flow change causing errors in the reported M and Re . These parameters can be corrected if the presence of fog is detected or observed, which is difficult to do with the present system employed to measure humidity in these facilities. To mitigate the presence of fog in the test section, AEDC spends a significant amount of energy, at a

considerable expense, drying the tunnel and making humidity measurements to determine if the tunnel flow is at an appropriate humidity level to proceed with the test. Thus, there is a need for a quicker, simpler and more robust way to make facility humidity measurements.

The current system used to measure humidity in these facilities is based on two CMHs, working in parallel, where a flow sample is extracted from the stilling chamber and fed into the CMH through plastic tubing. While this system has been the best way to make facility humidity measurements, it has a number of issues. First, the CMH's are slow to respond taking on the order of minutes to reach equilibrium and then output an accurate humidity measurement. Secondly, the mirror in each CMH frequently gets contaminated which prompts the instrument to perform a cleaning cycle which can take several minutes to complete, all while the test is put on hold while the facility is operating at a test condition. If the mirrors contamination becomes significant, then a more extensive cleaning procedure must be completed where they are cleaned manually, which takes even more time. It is also not uncommon to see the two CMH systems measuring differently, offset by a constant value, requiring test engineers to troubleshoot, wait to see if both systems agree and/or determine which measurement is more accurate. These inherent issues with the CMH system lead to a significant amount of time where the facility is on condition, but the test is on hold. Considering the operational costs of these tunnels are on the order of \$100K/day and test campaigns cost millions of dollars, developing a new measurement capability that can mitigate these issues can save the government and taxpayer an immense amount of money.

In addition to the issues discussed above, the CMH cannot be installed in the test section due to the disturbances the flow extraction tubes would cause in the flow. This means the CMH system will never be a viable solution to make in-situ humidity measurements or precisely detect

fog in the test section. Annual calibrations are also required of the CMH's, which adds another step required to maintain the system and extra maintenance steps are to be avoided if possible.

The maturation of near-infrared (NIR) telecommunications diode laser technology has enabled the use of those lasers types to make absorption measurements in gas flows, including H₂O species concentration measurements. This makes LDA spectroscopy an excellent candidate for the development of a simple, robust humidity sensor for ground test applications. This laser based hygrometer (LH) will enable non-intrusive, in-situ humidity measurements in the facility test section. It will also have a much quicker response of less than one second, require very limited maintenance/calibration and be able to operate throughout a test campaign reliably and without going offline. The work herein, describes development and testing of a prototype LH system intended to supplement and eventually replace the CMH systems in AEDC wind tunnel facilities.

Background

The origins of non-linear spectroscopy date back to the late 60's with the successful demonstrations of semiconductor lasers [14]. In the 70's, the work of C.K.N. Patel [15] to demonstrate non-linear saturation spectroscopy of H₂O with a tunable infrared (IR) laser showed promise for adequate frequency stability to achieve high resolution spectroscopy. A few years later Ronald Hanson, at Stanford University's High Temperature Gasdynamics Laboratory, used absorption spectroscopy to measure combustion gases. This work paved the way for in-situ combustion temperature and species concentration measurements using LDA spectroscopy, although not immediately due to laser limitations. The Pb-salt lasers used at the time were multi-

mode, operated in the 5-15 μm wavelength range, required cryogenic cooling, and generated very low optical power [14] which negatively impacted their usefulness.

With the development and refinement of Pb-salt semiconductor lasers as well as the implementation of efficient algorithms to evaluate the Voigt Function [16] [17], a significant amount of work was performed in the 1980's to characterize the absorption line intensities and line shape parameters. In 1980, Lowry and Fisher at Arnold Engineering Development Complex (AEDC) measured six carbon monoxide (CO) line strengths and three collisional broadening half-widths in the 300-600K temperature range [18]. Two years later, Lundqvist, Margolis and Reid measured several collisional broadening coefficients of six NO and eighteen O₃ absorption lines at 296K [19]. Additional work performed by Lowry and Fisher at AEDC in 1983 to measure four additional CO absorption lines helped characterize additional absorption lines [18]. These works along with that of many others during the period, including Dr. William Phillips at AEDC, led to the establishment and continuous improvement of the high-resolution transmission (HITRAN) absorption database [20] managed by Harvard University.

The Pb-salt lasers used during this period were state-of-the-art for the time, but still had some major issues. One issue was these lasers were only stable at very low temperatures and thus had to be cooled to cryogenic temperatures while in operation to prevent mode hop and wavelength drift. An example of this setup can be seen in the work conducted by H.C. Walker and W.J. Phillips at AEDC [21]. Another minor drawback of the Pb-salt laser was its tuning range limitation. Walker and Phillips reported a tuning range of 0.5 cm^{-1} in their work referenced above [21]. This was considered to be an acceptable tuning range for the time. However, as gas temperature and pressure increase the absorption features can widen beyond the

laser's tuning range resulting in an incomplete line shape measurement impacting accuracy when fitting models to the data.

In the late 80's and early 90's, Pb-salt type diode lasers were made obsolete by the introduction of more robust InGaAsP and GaAlAs type laser diodes. These lasers were able to access the 1.35-1.41 μm spectral range where strong low temperature H_2O absorption lines occur [22]. In addition to their enhanced spectral range, these lasers could operate at room temperature and provide much more optical power. Work by Arroyo and Hanson in 1993 demonstrated the capability of an InGaAsP laser in the measurements of water vapor concentration, temperature and line-shape parameters [22]. The laser operated at a wavelength of 1385 nm with an optical power output of 5mW, three orders of magnitude greater than the Pb-salt type lasers described above. A year later, a follow-on effort expanded on this work to measure multiple gasdynamic parameters in a shock tube [23] and demonstrated that high speed measurements at 10kHz could be achieved using a tunable diode laser.

However, there was still one major limitation at the time, fiber signal delivery. Thus, the laser, detector and optics used in both Arroyo and Hanson's works had to be enclosed in a nitrogen purged container to prevent incidental water vapor absorption from the room air. This requirement limited laser diode spectroscopy to a precisely controlled laboratory environment. Soon after the work described above, a combined effort involving Baer and Hanson, of Stanford, and Newfield and Gopaul, of NASA Ames, demonstrated a multi-species laser diode sensor that included fiber optic signal delivery [24].

Additional work in the 90's and early 2000's to define line shape parameters of numerous H_2O lines by Toth [25], Langlois [26] and Lepere [27] and numerous others contributed significantly to the available number and accuracy of H_2O lines for use in spectroscopic

measurements. In the late 90's, Physical Sciences Inc. developed an LDA humidity sensor under a Small Business Innovation Research funded project with AEDC. The system was originally designed for use in multiple locations including turbine engine test cells and wind tunnels according to unpublished project reports. The system was never implemented for regular use in a test facility. By this time, LDA spectroscopy was well established and while no major hardware developments enhancing the technique occurred, continuous refinements with analysis and data reduction were ongoing and the technique was being expanded to different environments.

In the last decade, a new class of semiconductor lasers have emerged that have extended LDA applications into the mid-IR. First demonstrated by Bell Labs in 1994 [28], the QCL has the ability span wavelengths from approximately 3.5 to 24 μm , achieve powers reaching into the tens of mW's [29] and operate at room temperature. The two primary types of QCLs mentioned in the literature for LDA applications are: Distributed Feed Back (DFB) and External Cavity (EC). The DFB QCL exhibits stable, narrow-linewidth, single-mode operation but are limited in tuning range to approximately 10 wavenumbers [30]. The EC QCL, which utilizes an external cavity to scan across a broad wavelength range are capable of tuning in excess of 100 wavenumbers [31], including mode-hop free tuning ranges of approximately 40-60 wavenumbers [31] [32]. While EC QCLs allow the user to span a much larger wavelength range, they are larger, more sensitive to vibrations and are more costly than DFB QCLs [30]. The continued maturation of QCL technology is generating many new opportunities for the use of LDA spectroscopy to interrogate multiple gas species at temperatures and pressures that have been previously unavailable. This includes the work done by Schultz, et al. at Stanford University measuring CO, CO₂ and H₂O in UVA's ethylene-fueled scramjet combustor [33].

For the work presented in this thesis, a QCL was not utilized. The absorption lines that were selected for this application, based on expected facility conditions, were around 1.4 μm which is well within spectral range of existing NIR telecommunications diode lasers. Additionally, a suitable diode laser was available for use, obviating the purchase of additional laser equipment. As similar non-intrusive laser based sensors are developed at AEDC for other test facilities, especially facilities such as the space chambers where very low temperature and pressure conditions exist, the need for QCL's, specifically DFB QCL's, will likely need to be utilized to interrogate the much stronger H_2O and other gas species lines that exist in the mid-IR.

CHAPTER II

THEORY

Laser Diode Absorption

The phenomenon of absorption behaves according to the Beer-Lambert Law which describes the relationship between light and the medium through which it is travelling, illustrated in Figure 2.

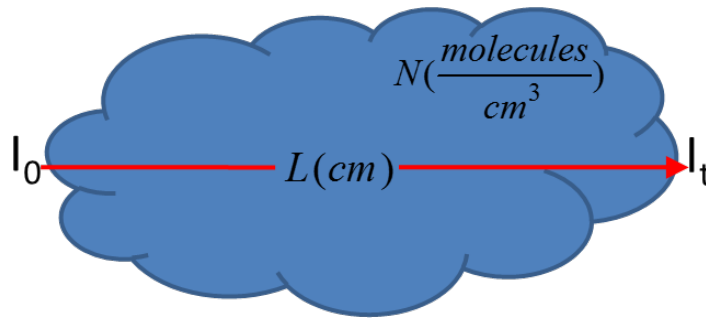


Figure 2: Beer-Lambert Law illustration

This law relates the intensity ratio of radiation from a collimated beam of light once it has passed through an absorbing medium, $I_t(\nu)$, to the incident beam, $I_o(\nu)$, with an exponential function.

The equation for this relationship can be written as:

$$\frac{I_t(\nu)}{I_o(\nu)} = e^{-\alpha(\nu)} \quad (1)$$

where $\alpha(\nu)$ is the spectral absorbance and ν is wavenumber, which can also be expressed as a wavelength or frequency using the relationship of these terms to the speed of light ($c=f\lambda=f/\nu$). The spectral absorbance, shown in Equation 2 below, can be expressed as the integral of the absorption coefficient, $k(\nu)$, along the path length, L , that the beam travels through the absorbing medium.

$$\alpha(\nu) = \int_0^L k(\nu) \cdot dl \quad (2)$$

Assuming the medium is homogeneous, which is a valid assumption for the work herein, the integral reduces into the following equation:

$$\alpha(\nu) = k(\nu) \cdot L \quad (3)$$

Furthermore, when the absorption is due to a single molecular absorption transition the absorption coefficient can be written as:

$$k(\nu) = S(T) \cdot \Phi(\nu) \cdot N \quad (4)$$

where $S(T)$ is the line strength, $\Phi(\nu)$ is the line shape function and N is the molecular number density.

The line strength parameter represents the magnitude of the absorption feature, is a function of temperature and can be described by the following expression:

$$S(T) = S(T_o) \cdot \frac{Q(T_o)}{Q(T)} \cdot \exp \left[-\frac{hcE''}{k_B} \left(\frac{1}{T} - \frac{1}{T_o} \right) \right] \cdot \frac{1 - \exp \left(-\frac{hc\nu_o}{k_B T} \right)}{1 - \exp \left(-\frac{hc\nu_o}{k_B T_o} \right)} \quad (5)$$

where $S(T_o)$ and $Q(T_o)$ are the reference line strength and total internal partition function referenced to a temperature, T_o , of 296 K [7]. $Q(T)$ is the temperature dependent total internal partition function which describes the sum of all of the energy modes (rotational, vibrational, electronic) or states contained within the absorption feature and is governed by the Boltzmann distribution [34] [35]. Planck's constant, h , the speed of light, c , lower energy state, E'' , Boltzmann's constant k_B , and the line center wavenumber, ν_o appear in Equation 5 as well.

The line shape function $\Phi(\nu)$, from Equation 4, is described by a Voigt profile. This is the convolution of two broadening mechanisms: Collisional and Doppler, which are the two dominant broadening mechanisms in atmospheric flight conditions [11]. In general, other line width influencing mechanisms exist, even though their effects are not considered in this work, such as: natural broadening, saturation broadening and broadening due to collisions with cell walls [36].

Collisional, or pressure, broadening is caused by intermolecular collisions that spread the frequencies of a spectral line [37]. When the absorptive medium's pressure exceeds 100 Torr, collisional broadening becomes the dominant broadening mechanism and the line shape takes a Lorentzian form [36]. Mathematically, collisional broadening is expressed by a Lorentzian line profile:

$$\Phi_c(\nu) = \frac{1}{\pi} \frac{\gamma_c}{(\nu - \nu_o)^2 + \gamma_c^2} \quad (6)$$

where γ_C is the Lorentzian line width at half-width at half-maximum (HWHM). Since the speed and frequency of intermolecular collisions is dependent on the temperature and pressure of the gas the Lorentzian line width is also dependent on temperature and pressure. The Lorentzian line width can be determined by scaling the line width to a reference line width, $\gamma_C^o(T_o, P_o)$, using temperature, pressure and the coefficient of temperature dependence, η . It is expressed by the relation below.

$$\gamma_C(T, P) = \gamma_C^o(T_o, P_o) \cdot \frac{P}{P_o} \cdot \left(\frac{T_o}{T}\right)^\eta \quad (7)$$

Additionally, the Lorentzian line width is dependent on the molecular species involved in the collision process. For species found in air, the broadening process can be approximated with a self-broadening term and an air-broadening term. The reference temperature and pressure are 296 K and 14.696 PSI, respectively. For water vapor in air $\gamma_C^o(T_o, P_o)$ can be expressed as:

$$\gamma_C^o(T_o, P_o) = X_{H_2O} \cdot \gamma_{SELF}^o + (1 - X_{H_2O}) \cdot \gamma_{AIR}^o \quad (8)$$

where, γ_{SELF}^o , γ_{AIR}^o and η can be found in the HITRAN database for a particular absorption line.

In addition, X_{H_2O} is the mole fraction of H₂O.

Doppler broadening is caused by molecular collisions that are driven by the thermal motion of molecules [38]. This type of broadening dominates at very low pressures when the effects of pressure broadening are negligible [36]. Doppler broadening is expressed by the following equation:

$$\Phi_D(\nu) = \frac{1}{\gamma_D} \cdot \sqrt{\frac{\ln(2)}{\pi}} \cdot \exp \left[-4 \cdot \ln(2) \cdot \left(\frac{(\nu - \nu_o)}{\gamma_D} \right)^2 \right] \quad (9)$$

where γ_D is the Doppler line width at HWHM;

$$\gamma_D = \frac{\nu_o}{c} \sqrt{\frac{2 R T \ln(2)}{M}} \quad (10)$$

where c is the speed of light, R is the ideal gas constant and M is the molar mass of H₂O.

The convolution of the Doppler and Lorentzian broadening mechanisms yields the Voigt function which can be expressed by the following equation:

$$\Phi(\nu) = \frac{1}{\gamma_D} \left(\frac{\ln(2)}{\pi} \right)^{1/2} \cdot \frac{y}{\pi} \cdot \int_{-\infty}^{\infty} \frac{e^{-t^2}}{(x-t)^2 + y^2} dt \quad (11)$$

where x and y represent the following respective expressions:

$$x = \frac{\sqrt{\ln(2)}}{\gamma_D} (\nu - \nu_o), \quad y = \sqrt{\ln(2)} \frac{\gamma_C}{\gamma_D} \quad (12)$$

The improper integral within the Voigt function shown above in Equation 11 cannot be solved analytically, but can be approximated for practical purposes. More detail on the evaluation of the integral will be presented in the next section.

Now by substituting 11 and 5 into 4, 4 into 3 and 3 into 1 yields the following expression for transmitted intensity.

$$I_t(\nu) = I_o(\nu) \cdot \exp \left\{ -S(T_o) \cdot \frac{Q(T_o)}{Q(T)} \cdot \exp \left[-\frac{hcE''}{k_B} \left(\frac{1}{T} - \frac{1}{T_o} \right) \right] \cdot \frac{1 - \exp\left(-\frac{h\nu_o}{k_B T}\right)}{1 - \exp\left(-\frac{h\nu_o}{k_B T_o}\right)} \cdot \frac{1}{\gamma_D} \left(\frac{\ln(2)}{\pi} \right)^{1/2} \cdot \frac{y}{\pi} \cdot \int_{-\infty}^{\infty} \frac{e^{-t^2}}{(x-t)^2 + y^2} dt \cdot N \cdot L \right\} \quad (13)$$

For this work, measuring water vapor in air, the reference values $T_o, S(T_o), Q(T_o), E''$ and ν_o are available from the HITRAN database and the other constants h, c and k_B are known.

Line Shape Function Approximation

Since the integral contained within the Voigt function, shown in Equation 13, has no analytical solution, an approximation must be used to solve the integral. One such approximation, developed by Kuntz [39], which is an optimization of previous work by Humlicek [17], expresses the Voigt function as the real part of the product of an exponential function and the complementary error function. The expression is shown below where $z = x + iy$ and x and y are shown in Equation 12.

$$\Phi(\nu) = \frac{1}{\gamma_D} \left(\frac{\ln(2)}{\pi} \right)^{1/2} \cdot \text{Re} \{ e^{-z^2} \cdot \text{erfc}(iz) \} \quad (14)$$

Equation 13 can now be re-constructed using the approximation shown in Equation 14 to eliminate the improper integral.

Final Computational Equation

The resultant equation from the previous section, discussed but not shown, is much easier to evaluate than Equation 13, but more work is required in order to obtain an expression that can be implemented into code. The expression must be completely expanded, as shown in Equation 16. The first step is to substitute Equations 14, 12, 7, 8, 10 and 15 into Equation 13 to fully expand all of the terms. The constant in Equation 15 is Loschmidt's number and represents the number of molecules in a given volume [cm^{-3}].

$$N = 2.6885 \times 10^{19} \cdot X_{H_2O} \left(\frac{P}{P_o} \right) \left(\frac{T_o}{T} \right) \quad (15)$$

Next, the numerical values for T_o , P_o , h , c , k_B will be substituted into the expanded equation discussed above leading to the final form of the mathematical model shown below in Equation 16. This will be implemented into the Spectral Model and Curve Fitting Tools discussed in the next chapter.

$$\begin{aligned}
I_t(\nu) = I_o(\nu) \cdot \exp \left\{ -S(296) \cdot \frac{Q(296)}{Q(T)} \cdot \exp \left[-1.438777661 \cdot E'' \left(\frac{1}{T} - \right. \right. \right. \\
\left. \left. \left. \frac{1}{296} \right) \right] \cdot \frac{1 - \exp \left(-1.438777661 \cdot \frac{\nu_0}{T} \right)}{1 - \exp \left(-1.438777661 \cdot \frac{\nu_0}{296} \right)} \cdot \frac{1}{3.5811 \times 10^{-7} \nu_0 \sqrt{\frac{T}{M}}} \left(\frac{\ln(2)}{\pi} \right)^{1/2} \cdot \right. \\
\left. \operatorname{Re} \left[e^{- \left\{ \frac{\sqrt{\ln(2)}}{3.5811 \times 10^{-7} \nu_0 \sqrt{\frac{T}{M}}} (\nu - \nu_0) + i \sqrt{\ln(2)} \frac{[X_{H_2O} \gamma_{SELF}^0 + (1 - X_{H_2O}) \gamma_{AIR}^0] \cdot \frac{P}{14.696} \left(\frac{296}{T} \right)^\eta}{3.5811 \times 10^{-7} \nu_0 \sqrt{\frac{T}{M}}} \right\}^2} \right] \cdot \right. \\
\left. \operatorname{erfc} \left(i \cdot \left\{ \frac{\sqrt{\ln(2)}}{3.5811 \times 10^{-7} \nu_0 \sqrt{\frac{T}{M}}} (\nu - \nu_0) + \right. \right. \right. \\
\left. \left. \left. i \sqrt{\ln(2)} \frac{[X_{H_2O} \gamma_{SELF}^0 + (1 - X_{H_2O}) \gamma_{AIR}^0] \cdot \frac{P}{14.696} \left(\frac{296}{T} \right)^\eta}{3.5811 \times 10^{-7} \nu_0 \sqrt{\frac{T}{M}}} \right\} \right) \right] \cdot 2.6885 \times 10^{19} \cdot \\
\left. X_{H_2O} \left(\frac{P}{14.696} \right) \left(\frac{296}{T} \right) \cdot L \right\}
\end{aligned} \tag{16}$$

It should also be noted that a numerical value for $I_o(\nu)$ has not been substituted; this will be discussed later in Chapter 3. Additionally, the exponential is carried through into the mathematical model which is important in order to not linearize and limit the model to only weak absorption. The following table is a summary of the variables in the equation above and how they are treated.

Table I: Variables list for Equation 16

Variable	Units	Definition	Treatment
$I_o(\nu)$	W/cm ²	Incident intensity	Fit Parameter, Provides baseline fit
$I_t(\nu)$	W/cm ²	Transmitted intensity	Measured by LH system
$S(296)$	cm ⁻¹ /(molecules·cm ⁻²)	Reference line strength at 296 K	Input, HITRAN
$Q(296)$	-	Reference internal partition function at 296 K	Input, HITRAN
$Q(T)$	-	Temperature dependent internal partition function	Known, Interpolated from table
E''	cm ⁻¹	Lower state energy	Input, HITRAN
T	K	Temperature	Input, Fit Parameter
ν_o	cm ⁻¹	Line center wavenumber	Input, HITRAN
M	g/mol	Molar mass	Input
ν	cm ⁻¹	wavenumber	Input, Determined from Etalon Constants
X_{H_2O}	mol H ₂ O/ mol air	Mole fraction of H ₂ O	Input, Fit Parameter
γ_{SELF}^o	cm ⁻¹ /atm	Self-broadened HWHM	Input, HITRAN
γ_{AIR}^o	cm ⁻¹ /atm	Air-broadened HWHM	Input, HITRAN
P	PSI	Static Pressure	Input, Fit Parameter
η	-	Coefficient of temperature dependence of air-broadened HWHM	Input, HITRAN
L	cm	Path length	Input

CHAPTER III

SPECTRAL MODEL AND CURVE FITTING TOOL

Spectral Model

In order to select the best absorption transition for the environmental conditions and design range of the water vapor concentration the sensor is expected to measure, a computational model using MATLAB and its graphical user interface (GUI) has been created. A screen shot of the GUI is displayed in the following figure. The purpose of this model is to accurately simulate the absorption spectrum over a desired wavelength range so the optimal absorption line(s) can be selected to produce the most accurate humidity measurement.

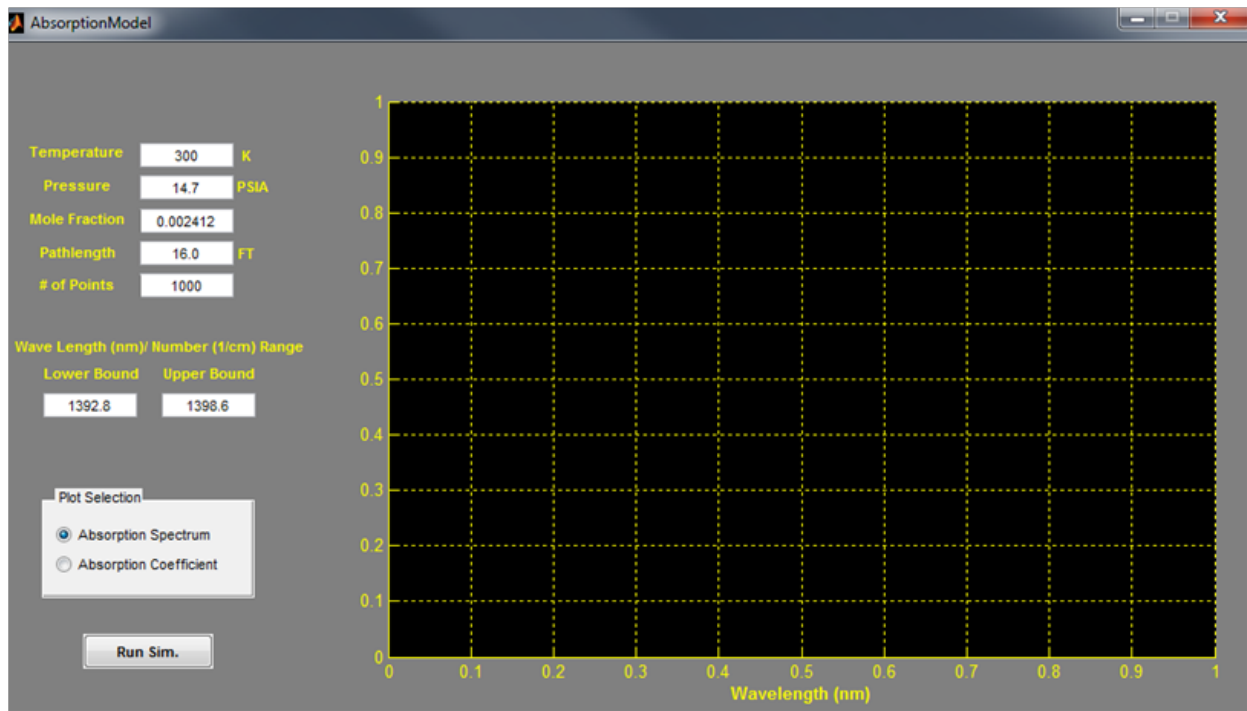


Figure 3: Absorption Model GUI

This model requires inputs for the environmental conditions which are to be simulated: temperature, pressure, H₂O mole fraction and path length. The spectral resolution, labeled as # of Points, as well as the lower and upper bound for the wavelength range are also inputs to the model. The bounds can be input as wavelength [nm] or wavenumber [cm⁻¹]. The GUI includes a plot selection option that allows the user to toggle between plots of the absorption spectrum (I) and the absorption coefficient (k). The button labeled “Run Sim.” computes the absorption spectrum and absorption coefficient over the selected spectral range for the given input environmental conditions and water concentration displayed the selected plot in the appropriate units.

When the GUI is launched, default values for all inputs are already selected. The line strength from Equation 5 and the Lorentzian linewidth from Equations 7-8 are calculated using the default values. If any of the environmental inputs are changed, the Lorentzian linewidth is updated as well. The path length is input in units of feet, but converts into centimeters for computation. When the lower or upper wavelength bound is changed, the program searches pre-loaded data from the HITRAN database to find all of the lines within the bounds. In the same step, the values for the reference line strength, $S(T_o)$, line center frequency, ν_o , self-broadened HWHM, γ_{SELF}^o , air-broadened HWHM, γ_{AIR}^o , lower energy state, E'' , and the coefficient of temperature dependence, η , are tabulated for each line found within the selected range. Upon pressing the “Run Sim.” button, the profile for each line within the range is calculated using the equations from Chapter 2. The lines are then summed spectrally to create the final spectrum over the specified range.

One very important aspect of the model is that each absorption line is modeled using a Voigt profile as expressed by Equations 11 and 12 in the previous chapter. The improper

integral in Equation 11 is approximated using Equation 14 as discussed in Chapter 2. However, as seen in Equation 16, this approximation is still very complicated since it deals with complex numbers. Thus several algorithms using various mathematical techniques have been developed over the years to perform the calculation [16] [17] [39] [40] [41]. While some of these techniques are faster and/or more accurate than others, the Humlicek algorithm [17], named after the developer, was selected due to its acceptable speed and accuracy. Implementation of this algorithm into the intensity equation is discussed previously in Chapter 2. A FORTRAN version of this algorithm [17] was converted into a MATLAB function for use in this work.

Absorption Line Selection

Currently, the HITRAN 2012 database has 12,952 different water absorption features in the 1.3-1.5 μm band which is of interest in this work due to the combination of strong water absorption features present and the laser sources that are readily available. Most of the absorption features overlap and interfere with each other when exposed to certain environmental conditions. Thus, it is imperative to choose features that will be suitable for measurement over the range of environmental conditions to which the sensor will be exposed. Literature on LDA describes systematic procedures for selecting the appropriate absorption lines and is outlined in papers by H. Li [4] and Farooq [42]. The procedure will vary slightly for each application, thus the conditions used in this work should be outlined.

The first condition, for the purposes of this study, deals with limiting the wavelength range of potential lines. This limit is governed by the availability of diode lasers operating within the 1.3-1.5 μm spectral range where H_2O absorption lines are present. The second condition addresses the line strength. The line strength must be strong enough to allow

measurable absorption, but not so large that the absorption line begins to saturate. The third and final condition is that the absorption feature must be sufficiently isolated from neighboring features. This is due to the fact that the analytical model used for the LH assumes a single absorption transition. If the tails of two features overlap significant errors can develop in the baseline fit, which is an important part of the fitting process which will be discussed in more detail in the next section.

Two specific absorption lines 1394.646 nm and 1395.0 nm, lines 10 and 11 respectively in Figure 4 below, were chosen for this work, based on the three conditions discussed in the previous paragraph. An illustration follows of how the absorption model GUI and criteria were used to select these specific absorption lines. The first condition discusses limiting the possible absorption lines within the wavelength range of the particular laser used. For this work, the available diode laser can be tuned safely over the range of approximately 1391 nm and 1397 nm. Operating the laser diode near the upper wavelength limits requires the laser to be operated near the temperature limits which can cause wavelength instabilities and can shorten the operational lifetime of the laser diode. The H₂O absorption spectrum for this wavelength range was generated by the spectral model and is displayed in the following figure.

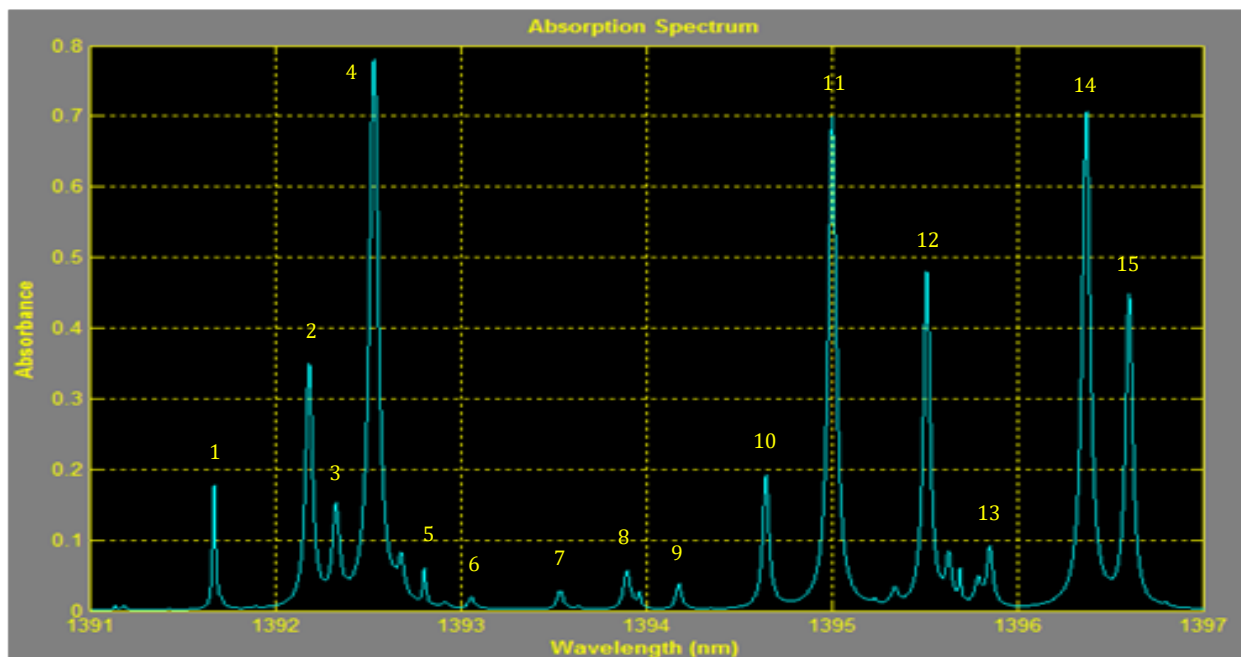


Figure 4: Absorption spectrum for H₂O between 1391 nm and 1397 nm at T=300 K, P=14.7 PSI, $X_{H_2O}=0.002412$ and L=16.0 ft

From this figure, fifteen discernible absorption features that have the potential to be used are identified within the wavelength constraints. Using condition two, features 3, 5-9 and 13 are eliminated due to the fact they are too weak. Condition three is now applied to the remaining features to assess the isolation of each feature. Of the remaining features 2, 4, 12, 14 and 15 all merge or have significant overlap with other features and are thus not good candidates for use in this work. This leaves features 1, 10 and 11 as potential candidates for use in the sensor. Further inspection into feature 1 reveals that an additional weak feature is present on the right wing, which was not visible in Figure 4 but can be seen in the following figure.

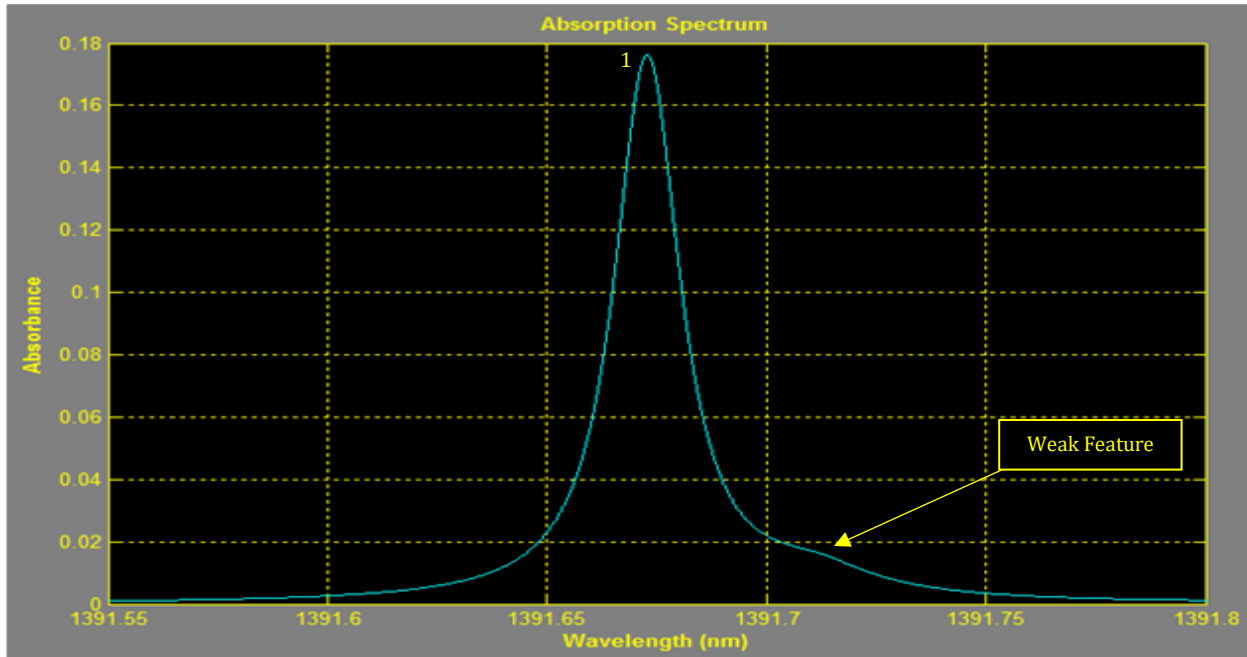
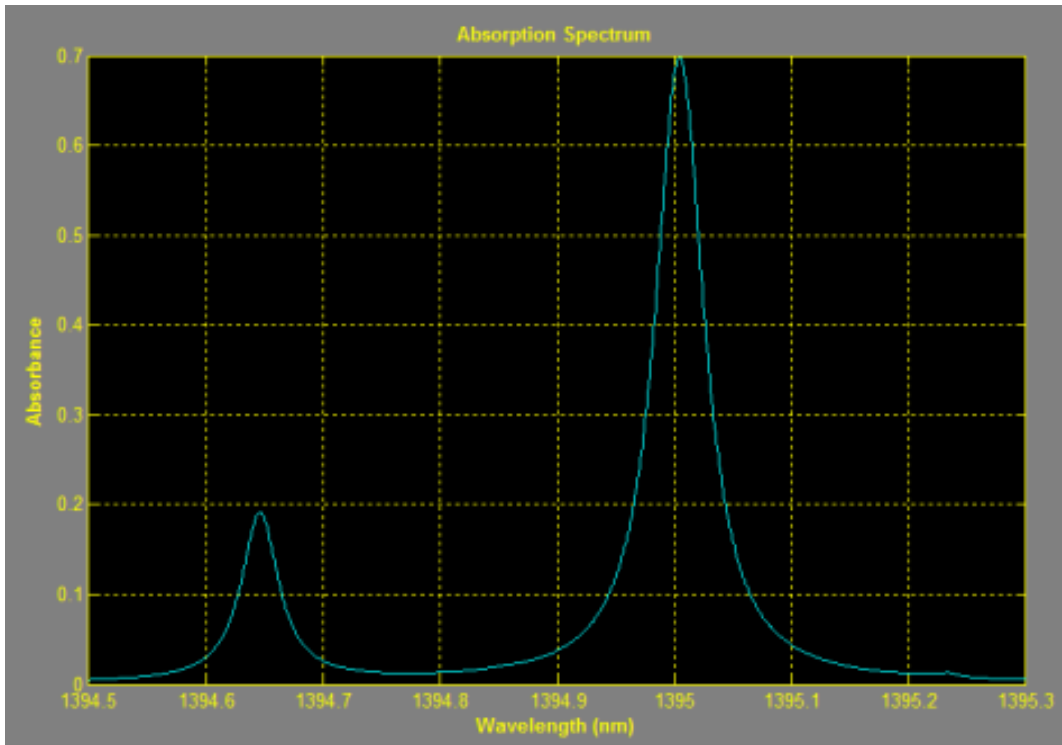


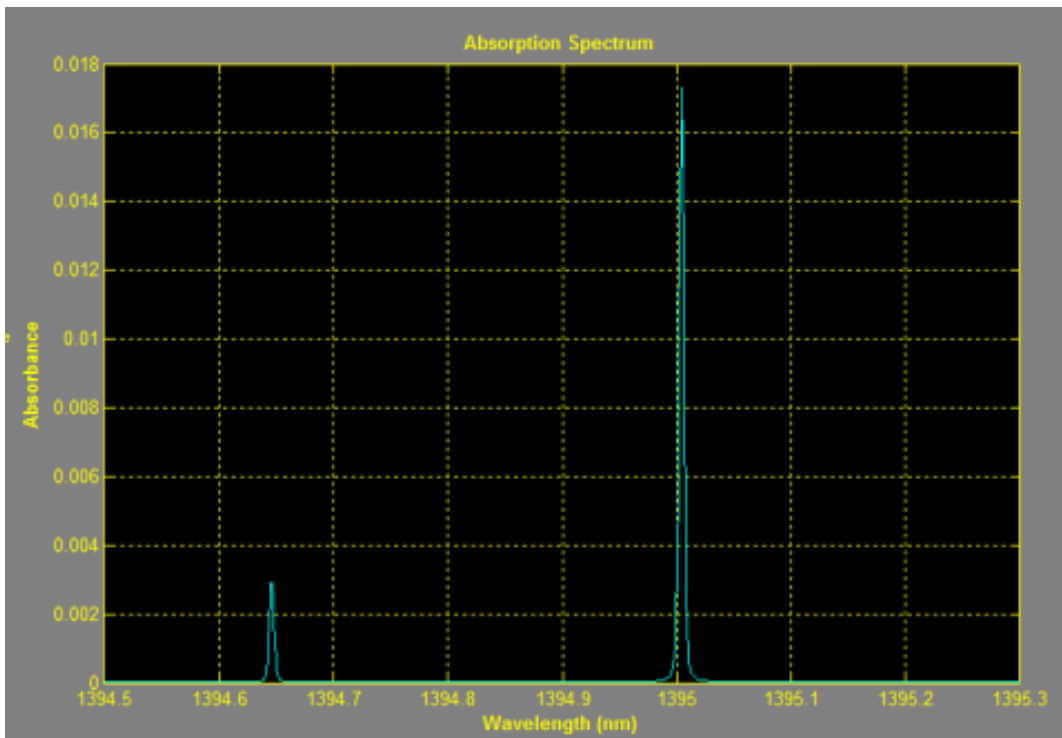
Figure 5: Absorption spectrum for feature 1 at T=300 K, P=14.7 PSI, $X_{H_2O}=0.002412$ and L=16.0 ft

This newly discovered feature will cause problems when trying to computationally analyze the profile and lead to significant error in the result. Next, features 10 and 11 were looked at in more detail to determine if the lines are suitable.

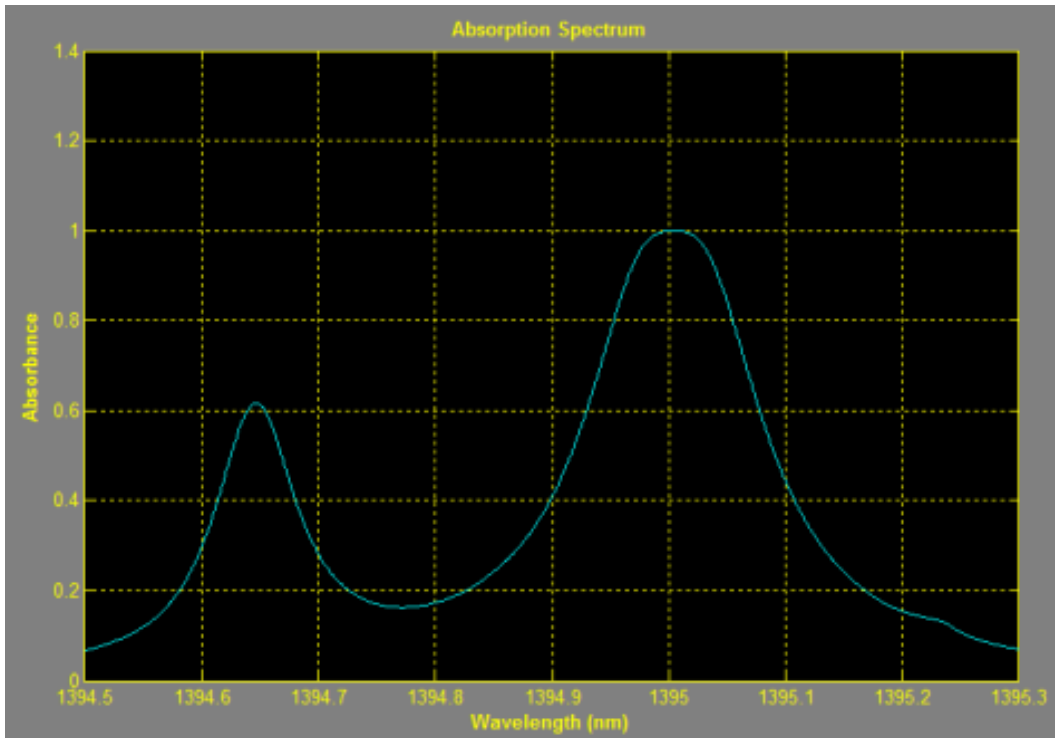
Features 10 and 11, at three different sets of environmental conditions, are displayed below in order to see how the different conditions affect the shape of each line.



(a)



(b)



(c)

Figure 6: Features 10 and 11, 1394.7 nm and 1395.0 nm respectively, for three different conditions. (a) T=300 K, P=14.7 PSI, $X_{H_2O}=0.002412$ and L=16.0 ft, (b) T=300 K, P=0.5 PSI, $X_{H_2O}=0.0001$ and L=16.0 ft and (c) T=300 K, P=27 PSI, $X_{H_2O}=0.01$ and L=16.0 ft

Figure 6(a) displays the two features at the same atmospheric conditions as Figures 4 and 5. The environmental conditions the two lines are expected to vary greatly from Figure 6(a). Figure 6(b) illustrates the effect of low pressure and humidity. Additionally, Figure 6(c) displays the effect of high pressure and humidity. In Figure 6(b), the line at 1394.7nm is too weak. This technique works best with lines ranging from at least 1% to approximately 80% peak absorbance. In Figure 6(c), the line at 1395.0nm is saturated. From Figure 6 it can be seen that one specific feature will not work for the given laser range and environmental conditions. At lower pressures, feature 10 will become too weak with maximum absorbance occurring around 0.3% and at higher pressures feature 11 will become too broad, spanning over 0.4 nm. To span

the dynamic range in concentration for the required temperature and pressure environmental conditions both lines must be used. Feature 10 will be used at high pressures and humidity levels, when feature 11 is too strong and broad. Similarly, feature 11 will be used at low pressures and humidity levels, when feature 10 becomes too weak and narrow. This will allow for an optimum line shape under all possible environmental water concentration conditions expected to occur within the facility. The HITRAN 2012 parameters used to describe these two lines are listed below.

Table II: HITRAN parameters for the 1394.7 nm and 1395.0 nm absorption lines

Parameter	1394.7 nm Line	1395.0 nm Line
ν_0	7170.27781	7168.43701
$S(T_0)$	1.969E-21	1.170E-20
γ_{AIR}^0	0.0928	0.0956
γ_{SELF}^0	0.5	0.473
E''	206.3014	173.3658
η	0.71	0.71

Curve Fitting Tool

Using the equations presented in Chapter 2, a curve fitting tool has been developed to fit the computational model to the raw test data. By fitting the environmental parameters, information regarding the test environment can be obtained. As with the computational model, MATLAB was used to perform this analysis via the creation of a GUI, which is shown in Figure 7. The GUI was developed for convenience and efficiency since a significant number of data sets need to be analyzed.

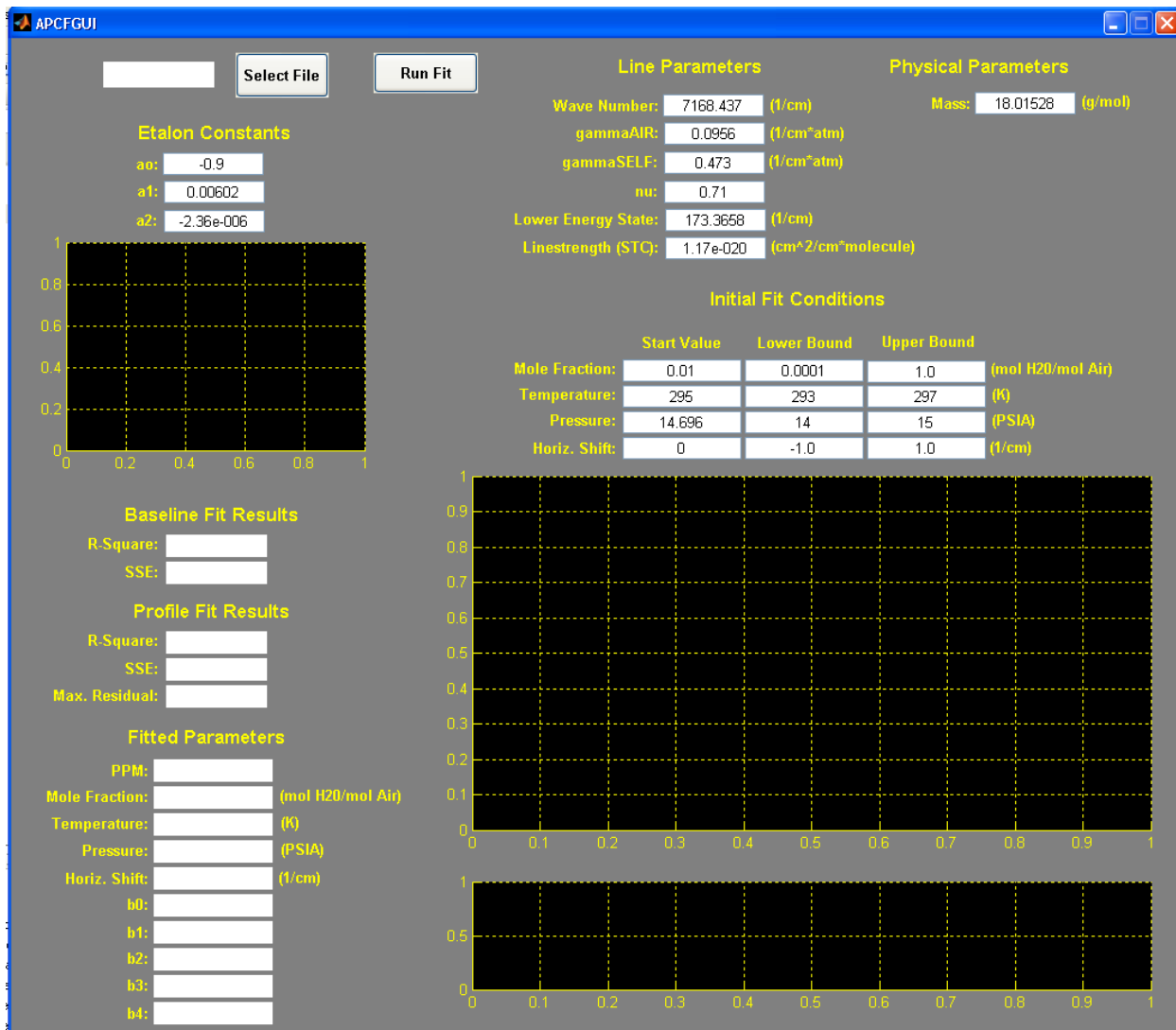


Figure 7: Curve Fitting Tool for raw absorption data

Figure 7 is clearly organized with the inputs located on the top half of the GUI and the outputs on the bottom half of the GUI.

To begin the analysis of a data set, the raw data must be loaded into the GUI's workspace using the Select File button. Once the button is pressed a file explorer will show up on the screen so that the appropriate data file can be selected. Once the file is selected, the raw data will be displayed in the plot in the top left corner of the GUI as seen in Figure 8.

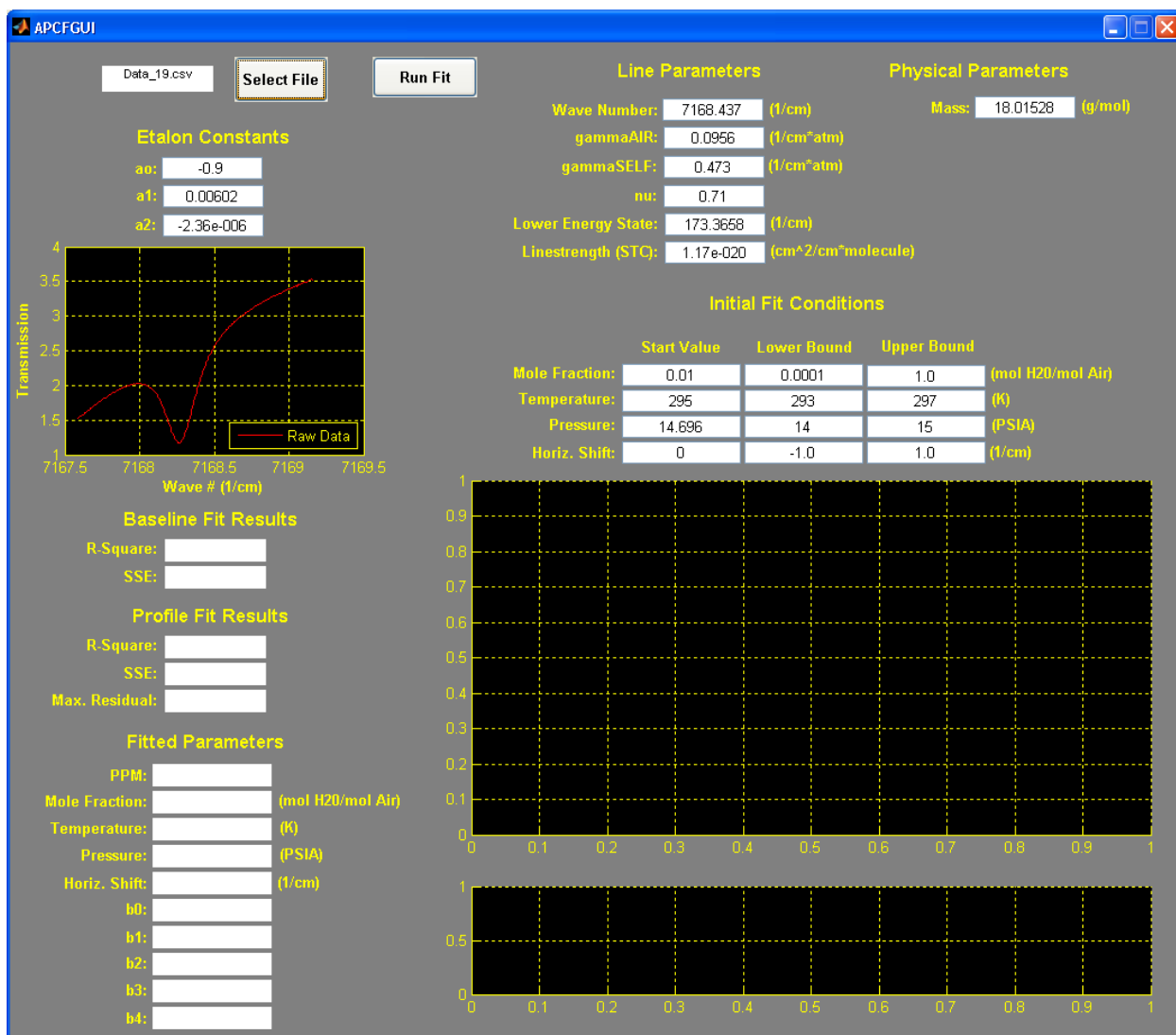


Figure 8: Curve Fitting Tool for raw absorption data showing raw data

However, the wavenumber axis in this plot will not be correct until the correct wavenumber calibration constants are input, which is done just below the Select File button via the edit text boxes. As updated values for the etalon constants a_0 , a_1 and a_2 are entered; the raw data plot will automatically update and will be correct once all correct constants have been entered for the appropriate absorption feature being measured. The three etalon constants are required for proper wavelength scaling and are obtained by directing the laser light at each wavelength

through a 2.0GHz etalon and measuring the peaks to achieve proper wavelength scaling for the raw signal generated from the detector. An example of this process is described below.

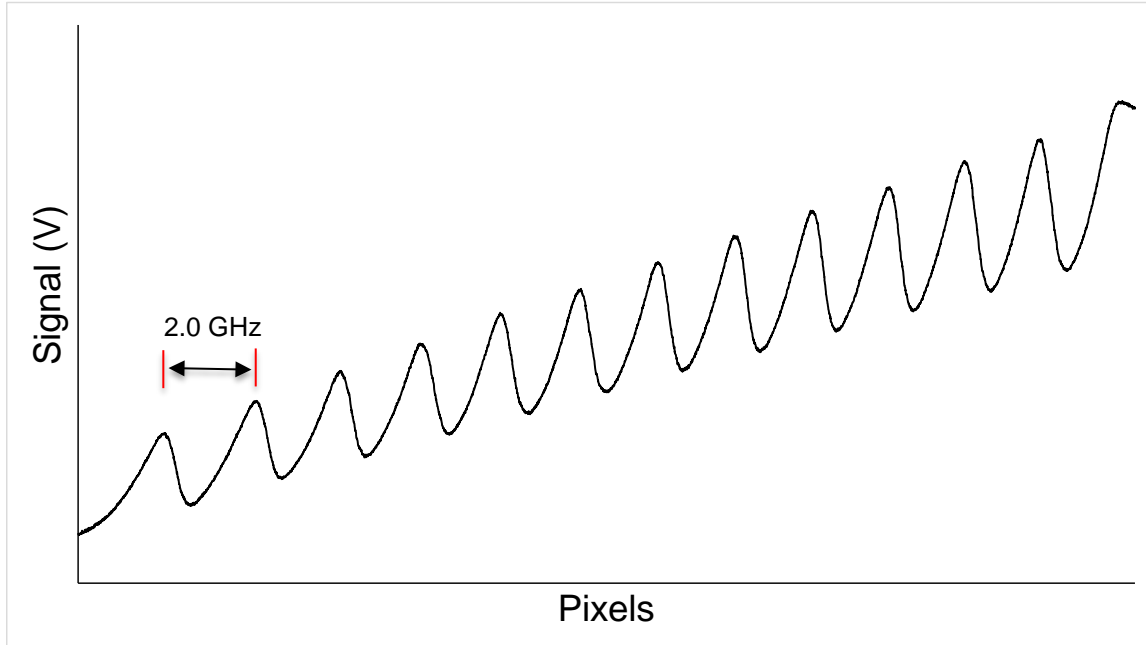


Figure 9: Example raw etalon signal

Figure 9 displays an example raw etalon signal for a single ramp sweep. By using a 2.0 GHz etalon, the wavenumber can be calculated using the relation $1/\lambda=f/c$. Next, the peak number (1-n) is multiplied by the wavenumber to obtain the relative wavenumber for each peak. Once the relative wavenumbers are calculated for each peak, the corresponding pixels at each peak can be determined. Next, the peak pixels (x-axis) and relative wavenumbers (y-axis) can be plotted then fit with a 2nd order polynomial curve fit. The three resulting coefficients are a_0 , a_1 and a_2 and are displayed in the table below for the two absorption lines used in this work.

Table III: Etalon constants for the 1394.7 nm and 1395.0 nm absorption lines

Parameter	1394.7 nm Line	1395.0 nm Line
a ₀	-0.95	-0.90
a ₁	5.46E-3	6.02E-3
a ₂	-1.27E-6	-2.36E-6

Next, all of the Line and Physical parameters must be checked and entered correctly.

These parameters are constants specific to the particular feature and species selected and are not a function of the environmental conditions that are being fit. Once all of the parameters are input and correct, the Initial Fit parameters must be adjusted as needed to ensure an accurate fit. These parameters represent the environmental conditions that affect the shape of the absorption feature and that are being fit in the tool, with exception to the wavenumber parameter. The wavenumber shift parameter has been added to the computational model to account for the wavelength drift of the laser diode or shift in the absorption line feature due to pressure or Doppler effects. This is done to create the most accurate fit possible. The Initial Fit Parameters each consist of a start value, lower bound and upper bound that guide the fit algorithm to most accurate solution possible.

Typically, the temperature is known to a high degree of accuracy and does not affect the feature nearly as much as the other parameters, so the upper and lower bounds are set very close to the start value. In addition, the pressure is also known to a fair degree of accuracy, but a generous range is usually selected to give the fitting algorithm enough freedom to produce a very accurate fit. In reality, the temperature and pressure are not unknown, but through trial and error, it is found that a much better fit is achieved by fitting these two parameters as well. The mole fraction is obviously the fit parameter in which we are most concerned with. It is unknown and

is very sensitive to the width and height of the feature, thus the upper and lower bounds create a very broad range for the same reason as the pressure parameter.

The type of fit used for this analysis is a non-linear least squares regression implementing the “large scale: trust-region reflective Newton” algorithm. Other non-linear least squares algorithms can be used in MATLAB including “Gauss-Newton” and “Levenberg-Marquardt.” In the literature, the “Levenberg-Marquardt” algorithm is mentioned most frequently, but for this work the above mentioned algorithm was used because it produced a much better fit and a more accurate mole fraction result.

In addition to the computational model itself, a fourth order polynomial fit has been added to fit the baseline I_0 . This way the computational model can be applied to the raw data without error. The polynomial expression is shown below where the b terms are the polynomial coefficients and $\Delta\nu$ is the wavenumber parameter mentioned above.

$$I_0 = b_0 + b_1 \cdot (\nu - \nu_0 + \Delta\nu) + b_2 \cdot (x - \nu_0 + \Delta\nu)^2 + b_3 \cdot (x - \nu_0 + \Delta\nu)^3 + b_4 \cdot (x - \nu_0 + \Delta\nu)^4 \quad (17)$$

The above expression is applied to the computational model by simply substituting the above expression for I_0 into Equation 16.

Once all of the inputs are entered the Run Fit button, to the right of the Select File button, is pressed to perform the fit. Upon completion, the raw data, the fit and the baseline fit are plotted on the large axis on the right. Also, the Fit results and Fitted Parameters are output to the left of the axis. The residuals of the raw data and fit data are plotted below the fit results plot

so that a visual representation of the fit accuracy can be observed. This can be seen in Figure 10 below.

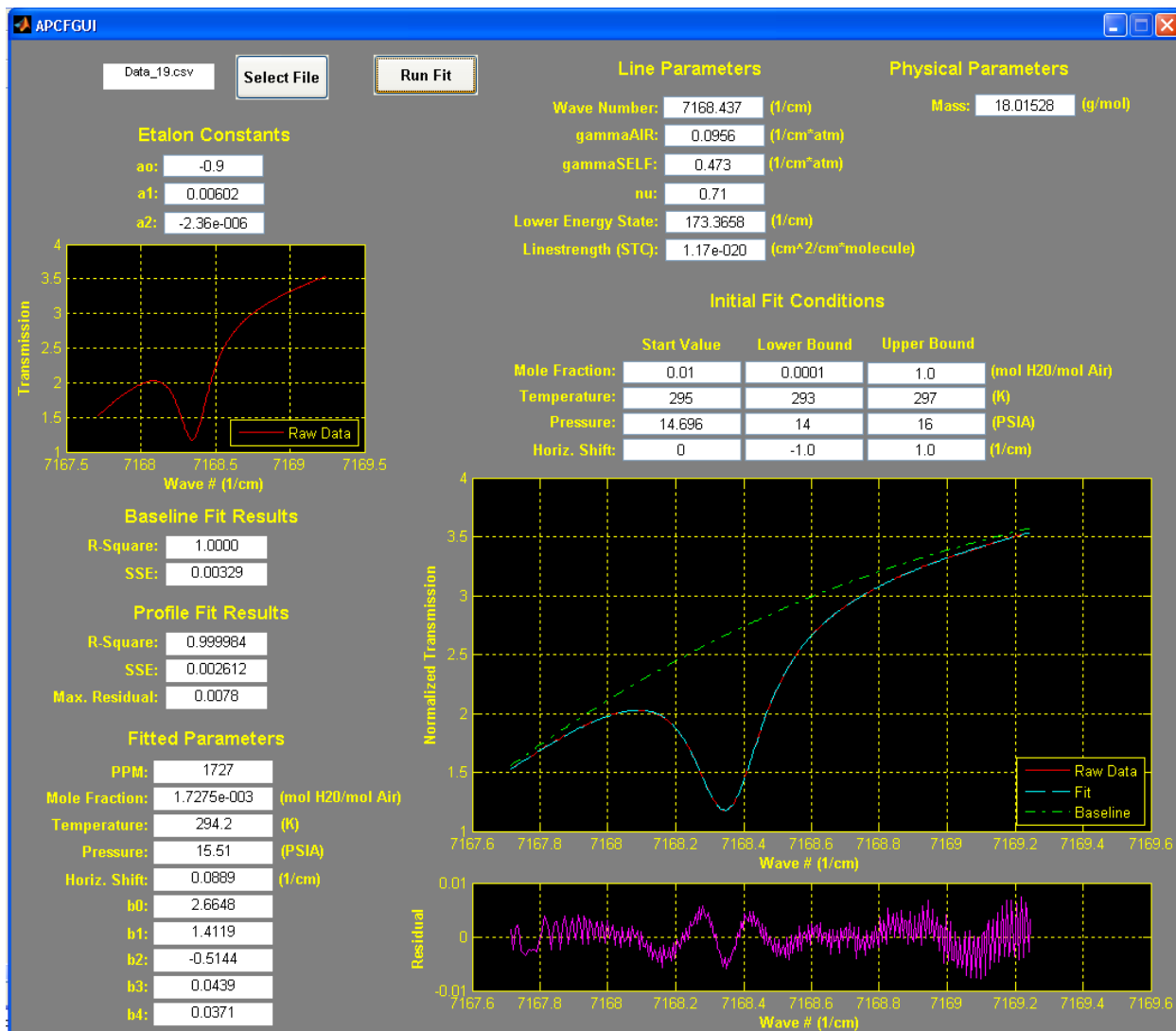


Figure 10: Curve Fitting Tool result for 1395.0 nm data set

CHAPTER IV

EXPERIMENTAL SETUP

Absorption Cell Setup

The absorption cell discussed here is a mechanism designed and built at AEDC to test and verify the operation of the LH against a CMH, which is considered to be the industry standard for measuring humidity. The humidity, pressure and temperature of the cell is adjustable and can be set to a specific point so that the entire range of environmental conditions that the LH System would expect to experience while in operation can be simulated. A schematic for the absorption cell experimental setup is displayed below.

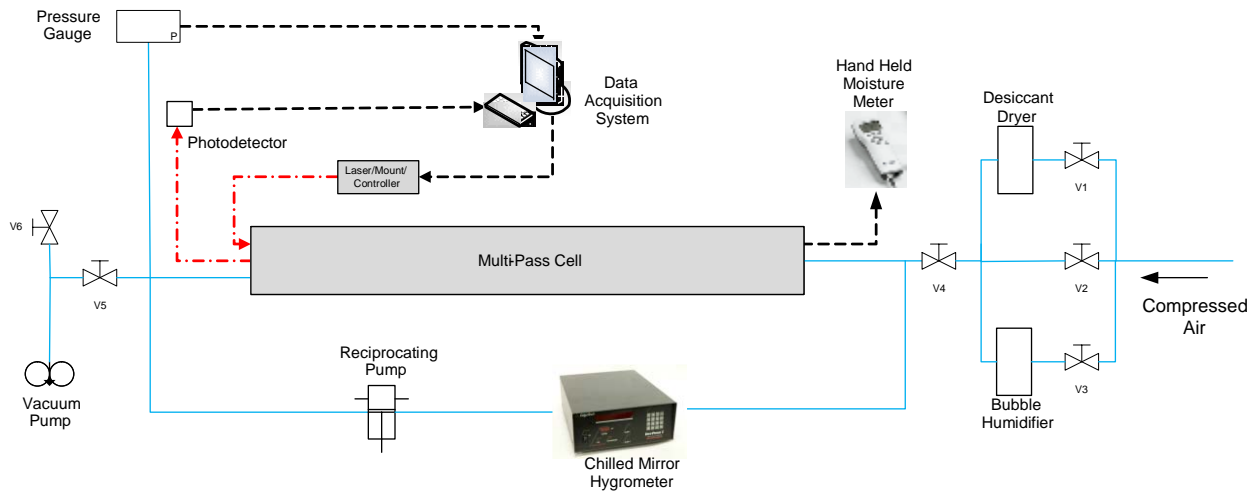


Figure 11: Absorption Cell setup

A compressed air source forces air into the setup through the air lines, depicted by a solid line on the right. Air can enter the circuit in one of three ways depending on the orientations of

valves V1-V3. If the air travels through valve V1, it passes through a desiccant dryer to reduce the amount of water vapor in the air. If air passes through V2 it enters the circuit unconditioned. If the air passes through valve V3, moisture is added to the air by a bubble humidifier. The conditioned/unconditioned air then travels through valve V4 to enter the circuit.

While conducting an absorption experiment, valve V4 will be closed to ensure the environmental conditions within the circuit will not change. The air is then circulated through the multi-pass cell, which has a total path length of 16 ft, by a reciprocating pump manufactured by Air Control, Inc. This is done to achieve a homogenous humidity level throughout the circuit. The pump is allowed to run for several minutes before any measurements are taken to ensure homogeneity. As the air circulates it passes through a Dew Prime III Chilled Mirror Hygrometer manufactured by EdgeTech, where the dew point of the air is measured. The pressure of the cell is measured by a PX32B1-050AV pressure transducer manufactured by OMEGADYNE, Inc. and displayed by a DP25B-S-A pressure Indicator manufactured by Omega Engineering, Inc.; both of which are represented by a single block in Figure 8. Valve V5 is used in the same manner as valve V4 while an experiment is being conducted, but can be opened so that a vacuum can be put on the circuit by a two stage vacuum pump, manufactured by Edwards, or the circuit can be exhausted to the atmosphere using valve V6. This allows for the pressure in the cell to be lowered or a vacuum to be applied. Valves V4 and V5 in combination with the compressed air supply and vacuum pump allow for complete pressure control of the circuit.

The tunable diode laser source produces continuous-wave radiation over an infrared spectral range of 1391-1397 μm which is contained and directed into the multi-pass cell using a single mode fiber optic cable, depicted by the dash-dot line. The signal beam is coupled into a 50 μm diameter, multimode fiber and routed to an InGaAs-PIN photodiode. The transmit and

receive fibers are both routed through a vacuum tight fitting installed on the absorption cell. The detector converts the optical signal into an electrical signal that travels to the data acquisition system (DAQ) via a National Instruments (NI) terminal block, TB-2709, which is directly connected to the NI DAQ model PXI-6123 analog to digital converter. The DAQ system is a 16 bit system capable of simultaneously measuring 8 separate channels at a rate of 500 KS/s, although only two channels were used in this work, raw data and pressure. The laser diode and temperature controller mount are a single unit, model LDCM-4371, manufactured by PSE Technology, which are controlled the by the DAQ computer as well. The injection current to the laser diode is modulated by a function generator using a sawtooth ramp. Temperature is manually input into the data acquisition system based on ambient room conditions and is considered to be a constant. An additional multi-pass cell humidity measurement is performed by a Hand-Held humidity and Temperature meter, model MM70, manufactured by Vaisala for comparison with CMH and LH.

Sensor Calibration Setup

Once it was confirmed that the LH functioned correctly using the lab absorption cell, described in the previous section, a calibration using a National Institute of Standards and Technology (NIST) traceable HG was performed. The experimental setup for the Precision Measurement Equipment Lab (PMEL) calibration is displayed below and will be discussed in further detail below.

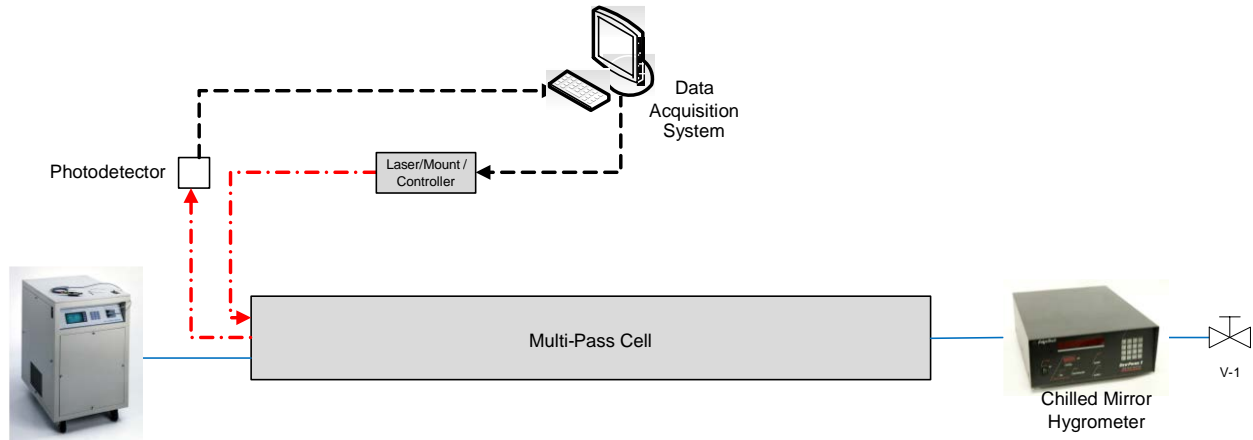


Figure 12: PMEL calibration setup

The humidity source is a Thunder Scientific Model 3900 “Two-Pressure Two-Temperature” Low Humidity Generator that is traceable to NIST. Once the desired dew point is set, the humidity source will begin producing air with the desired level of humidity. However, it does take the humidity source and absorption cell several hours to stabilize at the desired condition at the lower humidity levels. The air produced by the humidity source is directed into the calibration cell which is the same cell as used in the absorption cell setup. The air from the cell flows through a CMH and vented to the atmosphere. Once the humidity source and the CMH both stabilized a data point could be taken with the LH. The LH, in the above figure, is the same system used in the absorption cell setup and is described there.

Wind Tunnel System Setup

The actual operational system used in the wind tunnel is only a portion of what was seen in the Absorption Cell setup. The schematic for the operational system is shown in Figure 13.

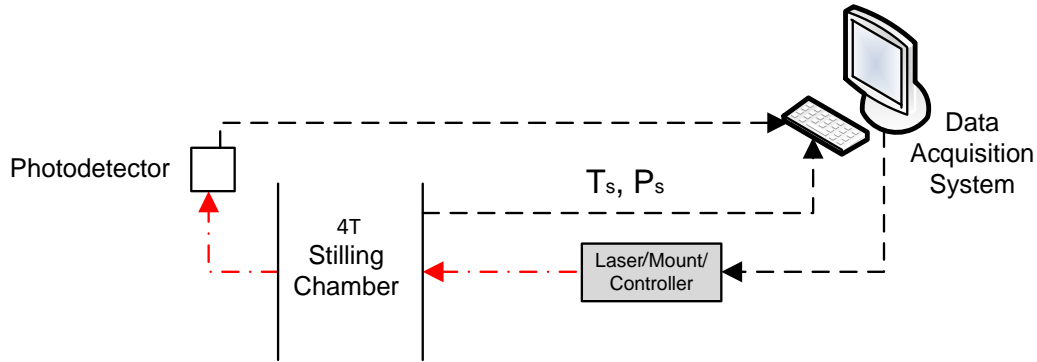


Figure 13: LH System setup

The laser diode and controller mount are the same as in the Absorption Cell and PMEL calibration setups. The beam is delivered to the wind tunnel via the same single mode optical fiber as in the absorption cell and calibration setups and is indicated by the dash-dot line. The exposed beam passes through the wind tunnel onto a photodiode which converts the laser beam into an analog signal and directs that signal into the same DAQ as in the absorption cell and calibration setups. It should also be noted that there are no pressure transducers or thermocouples displayed in Figure 13, this is because the static pressure and temperature are sent to the DAQ from the facility DAQ through a server.

CHAPTER V

EXPERIMENTAL RESULTS AND DISCUSSION

Absorption Cell Results

The first step in experimentation is to verify the operation of the LH which was done using the Absorption Cell described in Chapter 4. Figure 14 displays the LH results compared to the Viasala hand-held meter.

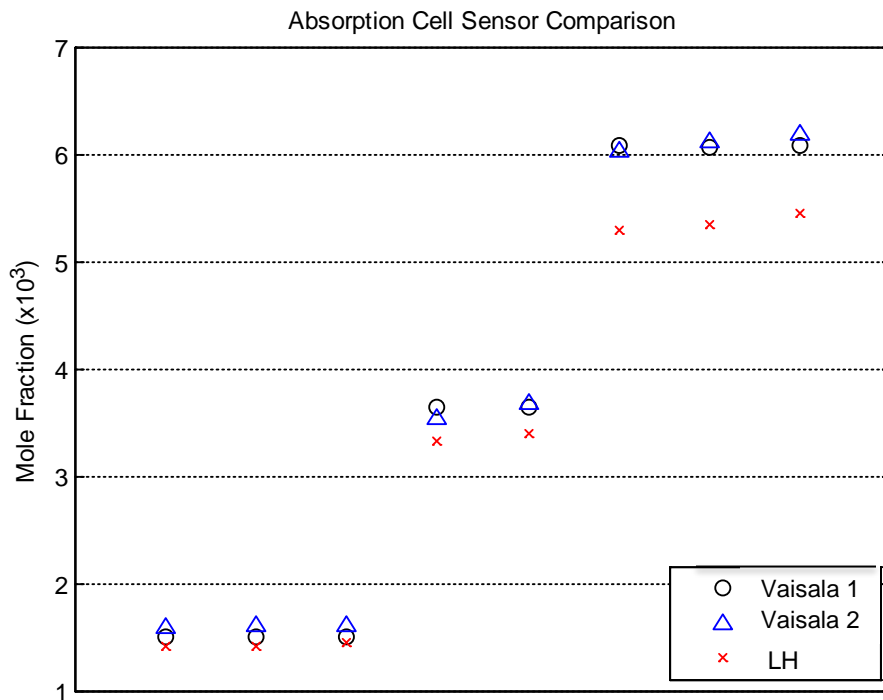


Figure 14: Mole fraction data for the Vaisala hand-held meter (2 channels) and LH for the 1394.7 nm absorption line

From Figure 14, it appears that Vaisala 1, Vaisala 2 and the LH agree at the lower humidity levels but the LH begins to differ from the Vaisala1, Vaisala 2 measurements as humidity level increases. It can also be seen that the LH consistently measures lower values than the Vaisala sensors.

Figure 14 shows that the LH and Vaisala measurements show the same trend, but there is discrepancy between instruments. Figure 15 shows this in more detail by comparing each of the Vaisala sensors to the LH.

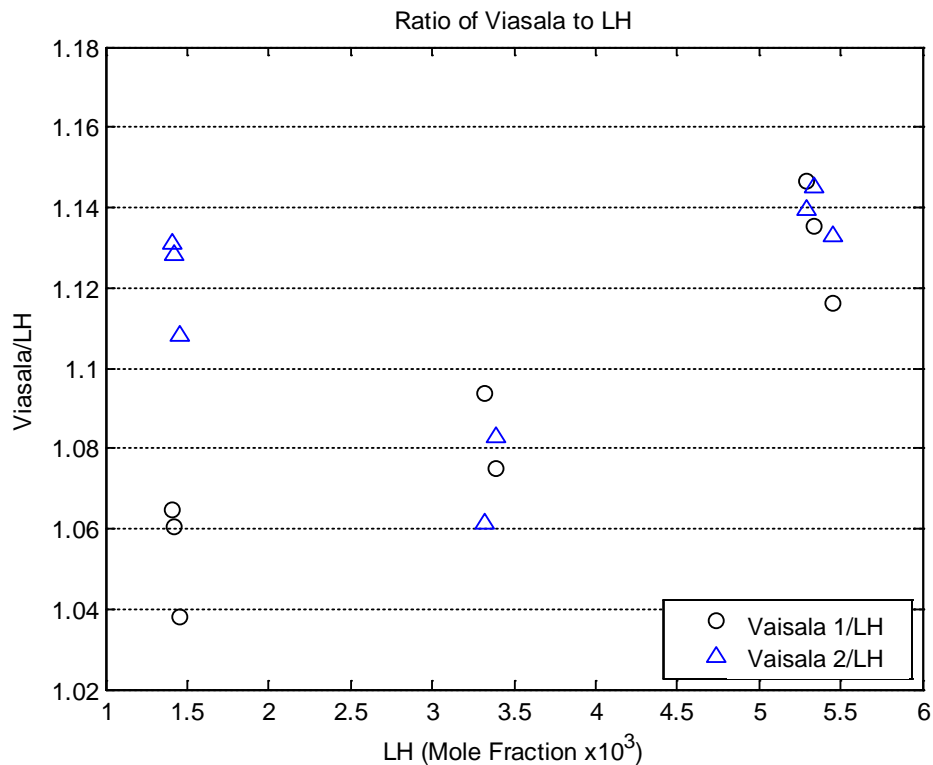


Figure 15: Vaisala/LH comparison for the Vaisala hand-held measurements for the 1394.7 nm absorption line

It can be seen in Figure 15 that all of the ratios are above 1, indicating the Vaisala sensors measure a higher humidity for the entire range of mole fractions seen in Figure 14. Additionally,

there appears to be more variability in the Vaisala measurements at lower humidity levels and less variability as humidity is increased. This shows that the Vaisala cannot precisely measure humidity in the 1,000 PPM range.

It was initially thought that the Vaisala hand-held meter would measure humidity accurately in the ranges created in the absorption cell, but its measurement discrepancy with the LH and its variability at lower humidity levels indicate otherwise. However, the same general trend is displayed with both the LH and the Vaisala hand-held meter. This provides confidence that the LH is operating correctly, but nothing can be concluded in terms of accuracy since there is no evidence that either device is correct. The next step is to add a CMH to the cell and compare the LH measurements to the CMH, which is considered the most accurate commercial humidity measurement device on the market.

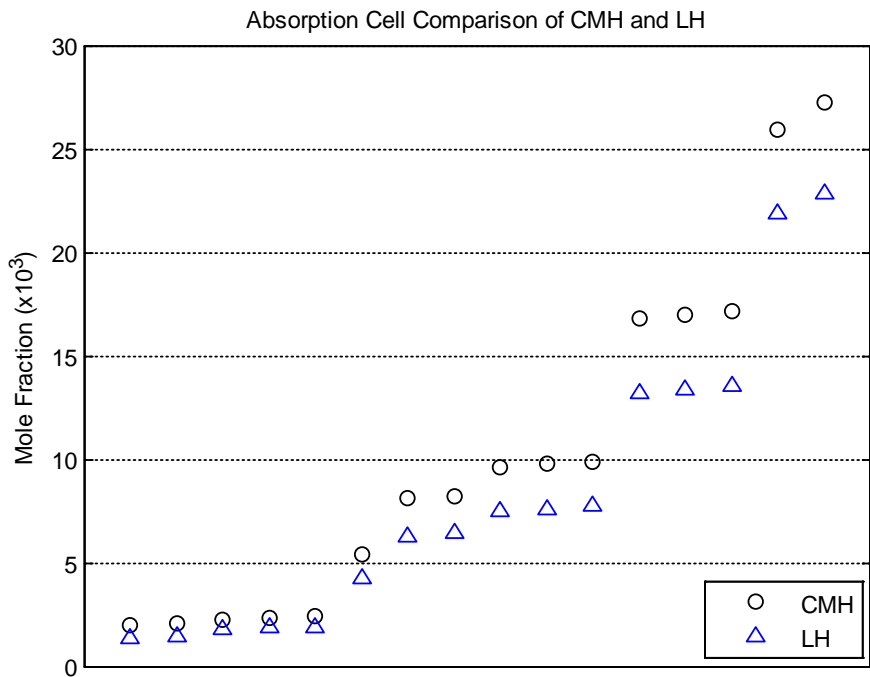


Figure 16: Mole fraction data for the LH and CMH for the 1394.7 nm absorption line

In comparing the LH to the CMH in the same manner as with the Vaisala hand-held meter above, the same general trend can be seen where there seems to be a good correlation between humidity measurements at lower humidity levels and increasing discrepancy as humidity increases.

Following the same logic above a direct comparison between the CMH and LH is shown below.

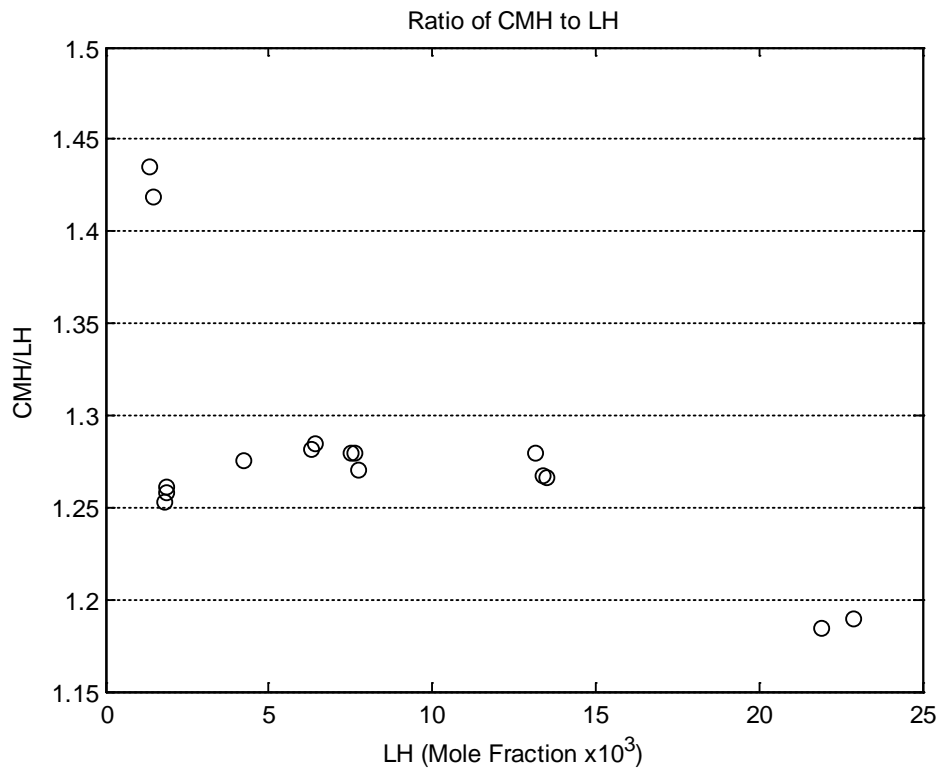


Figure 17: CMH/LH comparison for the 1394.7 nm absorption line

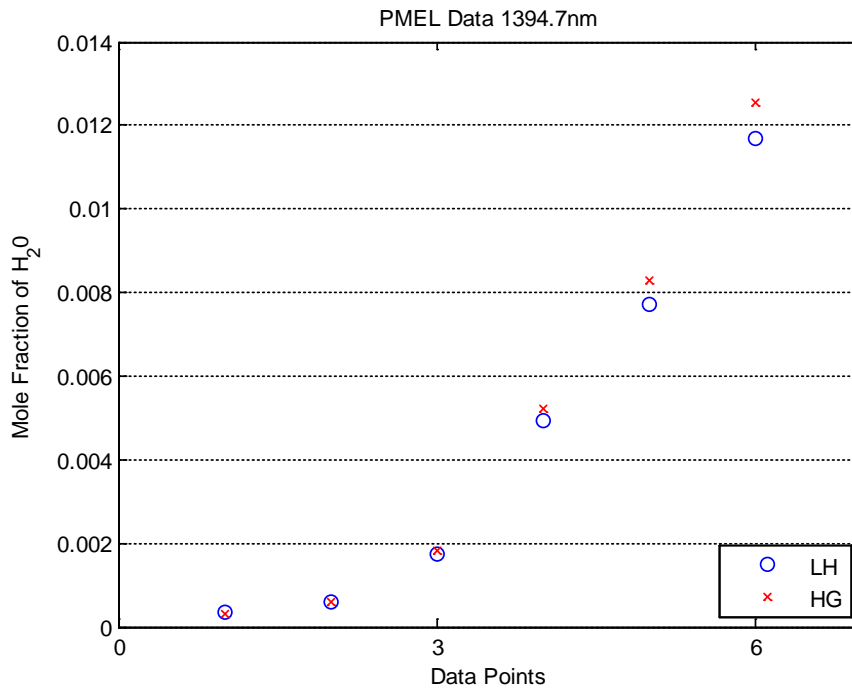
Again, the same trends can be seen with the CM/LH and Vaisala/LH comparisons. More discrepancy and variability between the devices appear at low humidity levels which decrease as humidity level increases. This is a logical result considering it is harder for devices to detect smaller amounts of humidity; however the humidity range generated by the absorption cell is

indicative of the environment the sensor would experience in operation so no information regarding the accuracy of the LH can be determined from the absorption cell measurements.

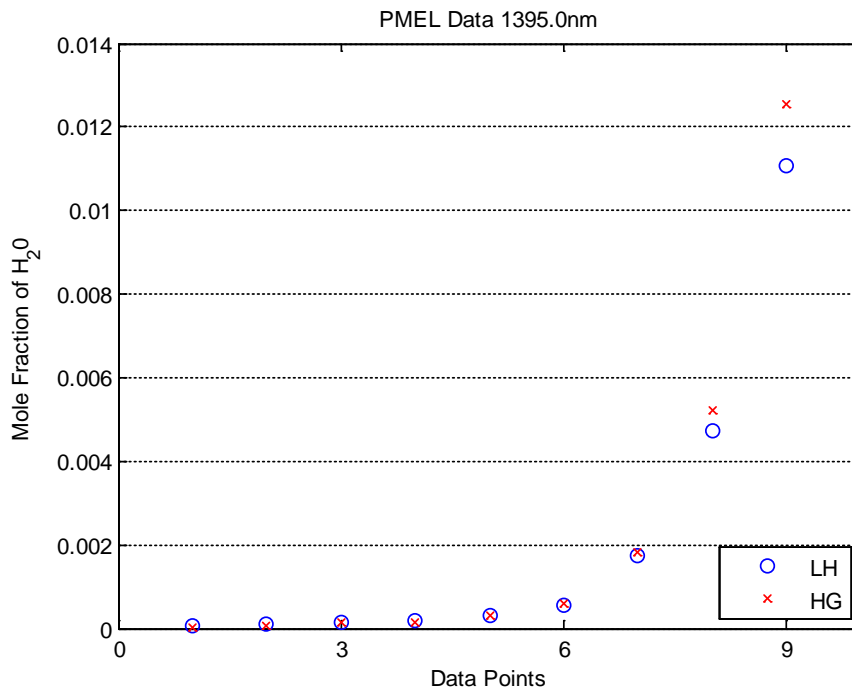
Overall the absorption cell measurements were successful in verifying that the LH device is operating correctly by the trend agreement with the Vaisala and CMH devices. However, with the Vaisala hand-held device measuring roughly 3-31% higher than the LH and the CMH measuring roughly 18-43% higher than the LH indicates that one or both of the devices is not accurate. Thus, a more thorough study of the accuracy of the LH device and possible calibration is required.

Sensor Calibration Results

The LH was calibrated over a X_{H_2O} range from 0.00004 to 0.01255. The 1394.7 nm absorption line was used for a X_{H_2O} range of 0.00031 to 0.01255 and the 1395.0 nm absorption line was used for a lower X_{H_2O} range of 0.00004 to 0.01255. Figure 18 shows the LH measurements at the HG set points.



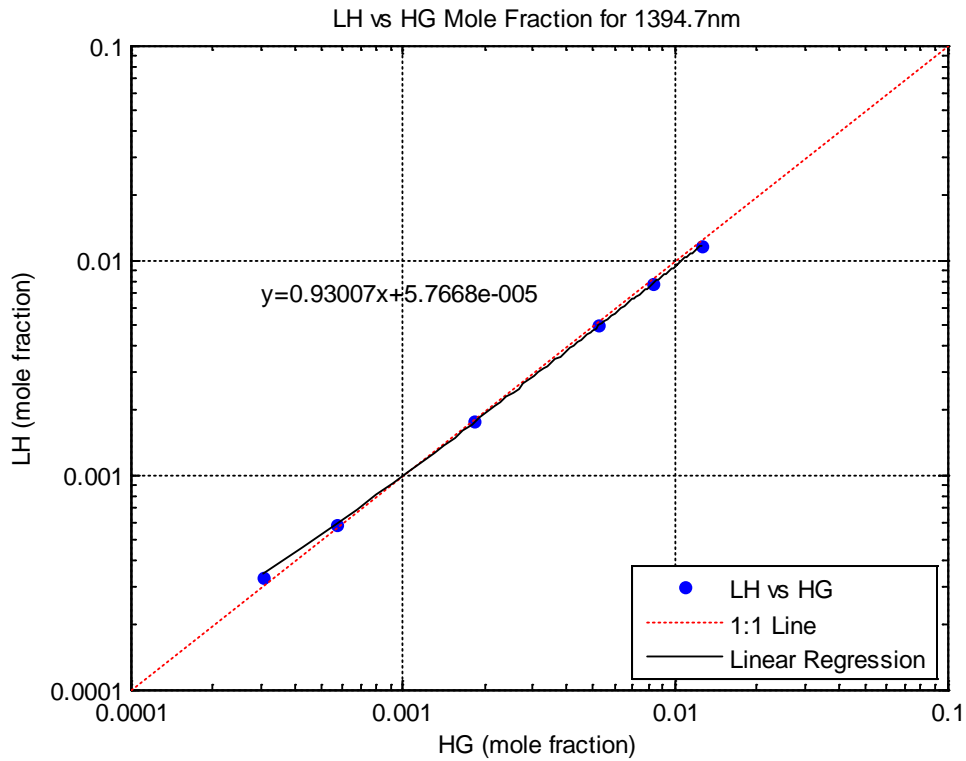
(a)



(b)

Figure 18: Mole fraction data for the LH and HG for two absorption lines (a) 1394.7 nm and (b) 1395.0 nm

From Figure 18, it appears there is good agreement between the LH and the HG. However, as the humidity level increases the LH under predicts the mole fraction for both absorption lines. To get a better look at the agreement between the two sources they can be plotted against each other using a log-log plot and a linear fit can be applied to see how close they actually agree.



(a)

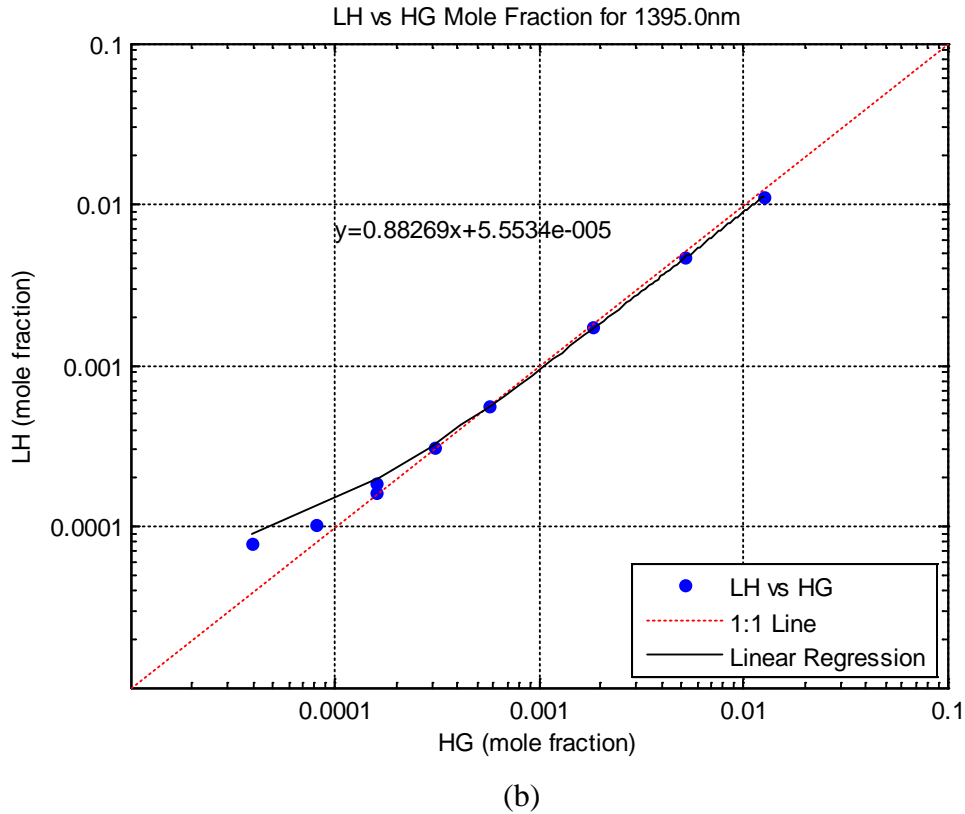
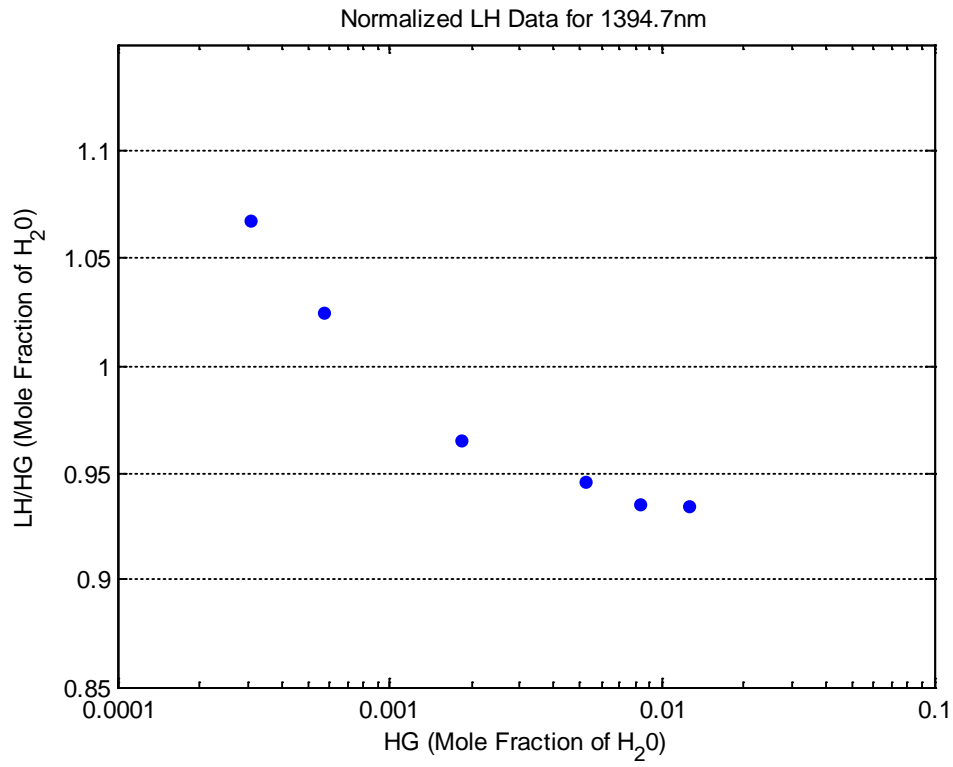


Figure 19: Log-Log plot of LH vs. HG for the two absorption lines (a) 1394.7 nm and (b) 1395.0 nm

From the linear fits it can be seen that the LH measurement using the 1394.7 nm line is in closer agreement with the HG. The slope over the entire humidity range of each line is 0.9301 and 0.8827 respectively. The 1394.7 nm line strength is 6X weaker than the 1395.0 nm line so it cannot measure as small of a mole fraction as the 1395.0 nm line, but over the range of mole fractions that were measured it has better agreement. It can be seen in Figure 19(b) that when the mole fraction drops below 0.0005, the LH response becomes non-linear and the relative error increases as the humidity decreases. It also appears that not only is the LH under-predicting at higher mole fractions, the LH is over-predicting at the lower mole fractions. This can be seen by comparing the data points and linear regression line with the 1:1 line in Figure 19 above.

Another way to view this is to look at the slopes of the above plots by dividing the mole fraction of the LH by the mole fraction of the HG, which would be the result if they were both measuring the same. This is done in the Figure 20.



(a)

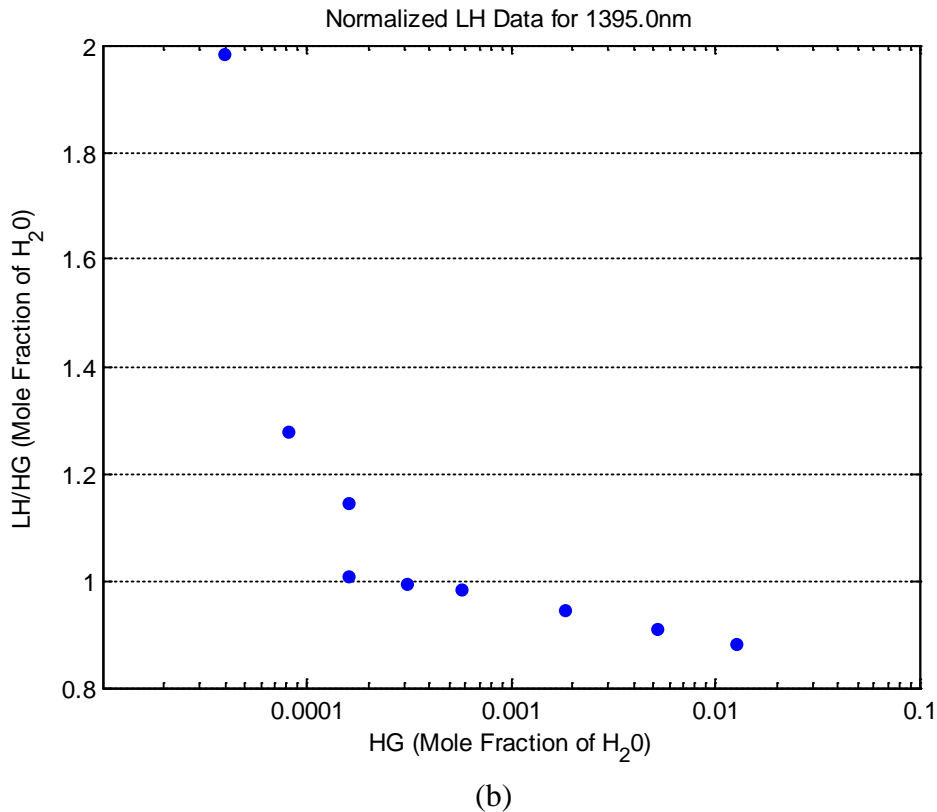


Figure 20: LH/HG vs. HG for (a) 1394.7 nm and (b) 1395.0 nm

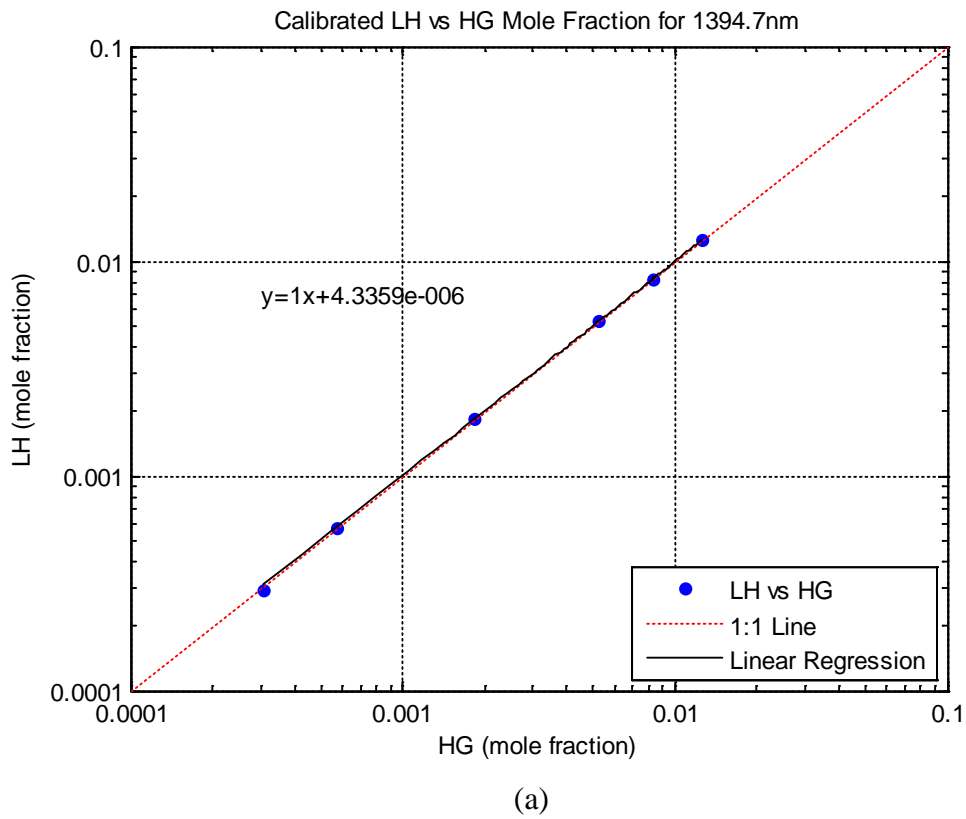
From Figure 20, the same trend noticed in Figure 18 can be viewed in more detail. The LH consistently over predicts mole fraction below approximately 0.001 and consistently under predicts mole fraction above 0.001 for both absorption lines. As the mole fraction drops below approximately 0.0016, the 1395.0 nm line begins to grossly over predict the mole fraction. However, the LH using both absorption lines under predict within 10% of the HG over the entire range of points taken above a mole fraction of 0.001 except for the highest mole fraction measurement for the 1395.0 nm line.

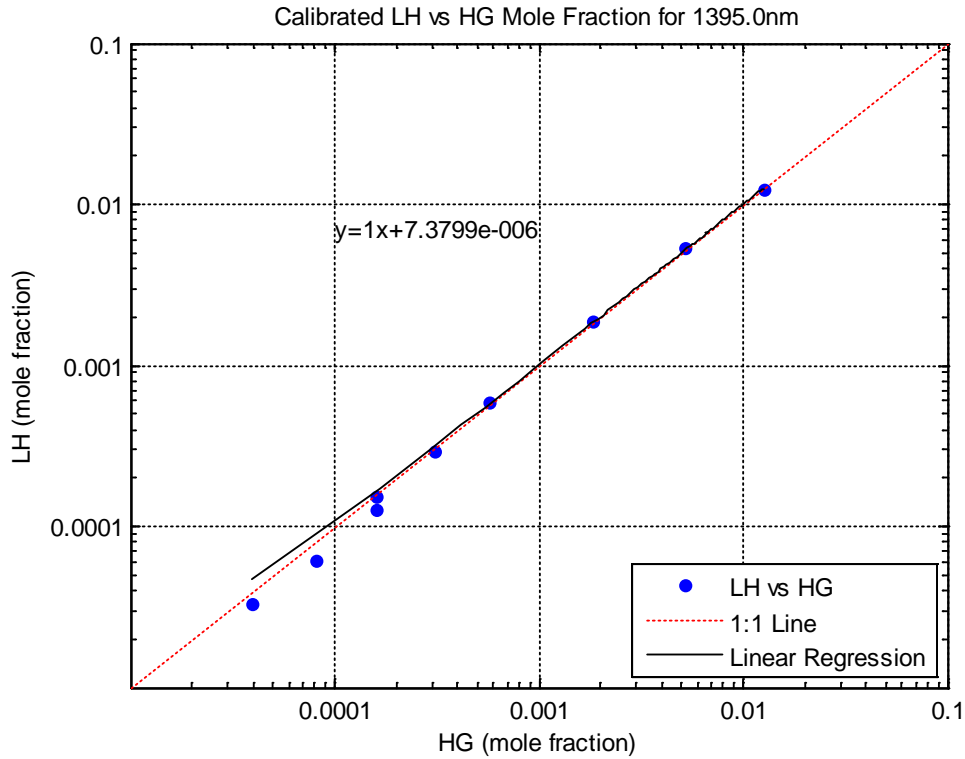
To correct this, the linear fit shown in Figure 19 above can be used to calibrate the LH. With a slope of 1 being perfectly calibrated, the linear fit can be converted into a calibration function by solving for x. The resulting calibration functions are shown below.

$$x_{1394.7} = 1.07519y - 6.2004e^{-5} \tag{18}$$

$$x_{1395} = 1.13290y - 6.2914e^{-5}$$

The uncalibrated results from Figure 19 can now be calibrated using Equation 18. The result is shown in Figure 21 below.





(b)

Figure 21: Log-Log plot of Calibrated LH vs. HG for the two absorption lines (a) 1394.7 nm and (b) 1395.0 nm

From Figure 21, the slope of the linear fit is now 1 indicating the calibration was successful in correcting the trend of LH overshoot at lower mole fraction and undershoot at higher mole fraction as discussed previously. However, it can be seen that some of the data points still do not fall along the fit line. This suggests that there is still some error associated with the system that cannot be calibrated out.

The remaining error can be broken down into two components: systematic, which quantifies error in the experiment or instruments used to make the measurements, and random error, which quantifies unknown changes or fluctuations in the experiment that cannot be predicted. Both types of error are present in the calibration and will be considered. The systematic error originates from the HG and is given by the manufacturer. The random error

originates from the linear curve fit discussed above. The total uncertainty can be calculated by squaring the systematic and random errors, adding them, then taking the square root. The following table shows the X_{H_2O} error values and the total X_{H_2O} uncertainty for this calibration procedure.

Table IV: Error component and total uncertainty values for PMEL calibration

	Systematic Error	Random Error	Total Uncertainty
1394.7 nm line	8.9359E-6	6.5669E-6	1.1089E-5
1395.0 nm line	8.9359E-6	1.5522E-5	1.7910E-5

The total uncertainty reported above indicates the PMEL calibration is accurate to a X_{H_2O} of $\pm 1.1089E-5$ for the 1394.7 nm line and $\pm 1.7910E-5$ for the 1395.0 nm line or approximately 11 and 18 PPM respectively.

It should also be noted that the CMH's have a dew point temperature measurement accuracy of $\pm 0.2^\circ\text{C}$ ($\pm 0.36^\circ\text{F}$), as stated in the operator's manual. This equates to a X_{H_2O} uncertainty of ± 0.000087 or ± 87 PPM at a total pressure and temperature of 1 atm and 75°F respectively, which is typical for the 4T tunnel. However, through extensive testing at AEDC a dew point uncertainty of $\pm 2^\circ\text{F}$ has been observed at best. This equates to a X_{H_2O} uncertainty of ± 0.000481 or ± 481 PPM at the same total conditions stated in the previous sentence.

From the PMEL results in Figure 19, it can be seen that the LH curve fitting tool has difficulty in fitting the absorption at very low and very high absorbance. For low humidity, the absorption signal is weak and the baseline noise degrades the fitting process. At high humidity levels, the absorption signal begins to saturate and interference from adjacent lines corrupt the baseline and degrade the curve fit since only one absorption feature is being analyzed.

The LH should be designed using an absorption line with larger line strength, the 1395.0 nm line, to measure the smaller mole fraction conditions and switch to a weaker absorption line, the 1394.7 nm line, to measure larger mole fraction conditions to prevent detector saturation. Thus, the number of different absorption lines used in the system design depends on the mole fraction range your sensor would be exposed to. Ideally, the sensor would be designed so that only one absorption line would be needed to cover the range of mole fractions the system would observe, however the larger the mole fraction range the lower the probability of using one absorption line is. This is why the absorption model is such an important tool in designing a LH so that mole fraction range limitation can be tested for each absorption line.

Wind Tunnel System Results

Based on the expected levels of water vapor and the PMEL results, the 1394.7 nm line was selected for use in AEDC's 4T wind tunnel. Details regarding the experimental set-up were previously discussed in Chapter 4. The raw and calibrated LH data are discussed below along with the calibration method and compared to the values from the CMHs currently installed and in use. The data was obtained during a wind tunnel test over a Mach number range from 0.9 to 2.5 where numerous different test conditions were set.

Figure 22 shows the calibrated LH and averaged CMH measurements for the AEDC 4T wind tunnel.

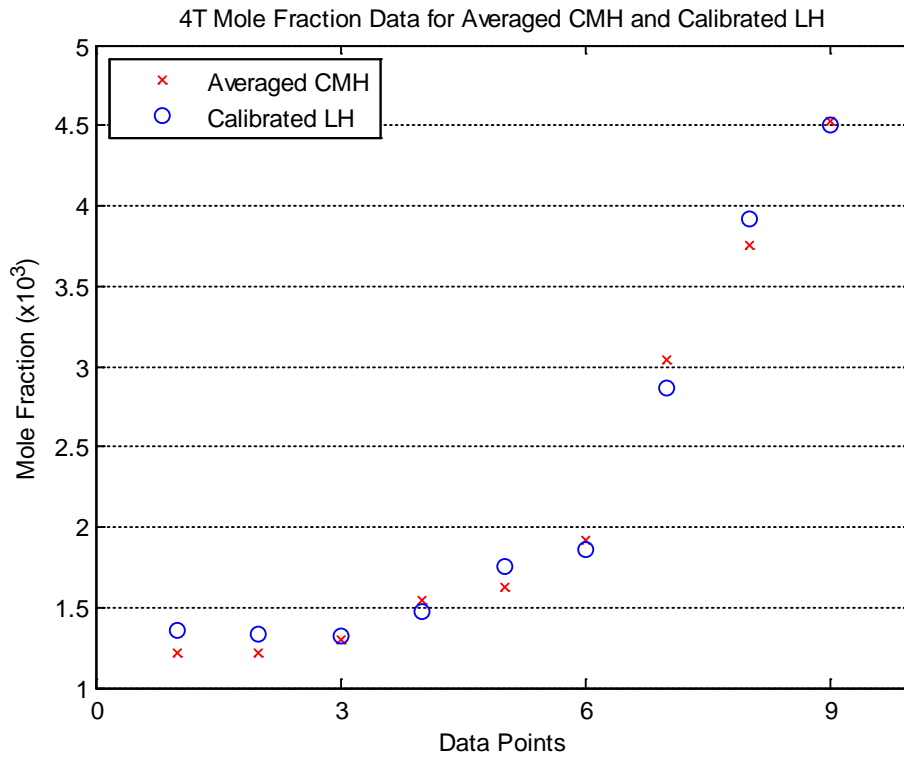


Figure 22: 4T mole fraction data for Averaged CMH and Calibrated LH

In comparing the averaged CMH and calibrated LH measurements, it can be seen that there is good agreement between the two systems over the entire range of mole fractions. Following the same logic as in the previous section, the two systems can now be plotted against each other and a linear fit can be applied to see how closely they actually agree.

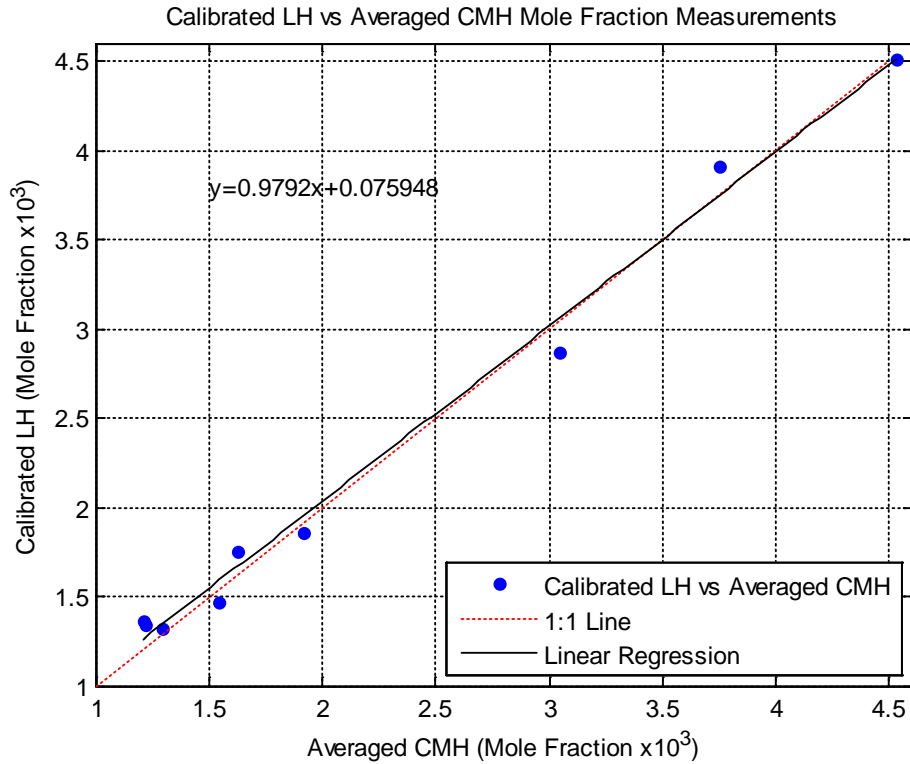


Figure 23: Calibrated LH vs. Averaged CMH mole fraction measurements

The calibrated LH is now measuring within approximately 2% of the CMH. This is a very promising result considering the CMH values shown are averaged and do contain variability within themselves. This result does verify that the LH system is quite capable of making accurate flow humidity measurements. In addition, this result demonstrates an instrument calibration against a NIST traceable humidity source. System calibration will likely only need to be performed once every year for each absorption line used unless the system is used to make measurements in different humidity conditions.

CHAPTER VI

CONCLUSION

Summary of Research and Results

The work contained within this thesis represents the incremental development of an LH system. The work began with the selection of an absorption line through the development of an absorption model. Next a non-linear regression analysis algorithm was created and used to validate the system using data from the lab absorption cell. The system was then calibrated using a NIST traceable HG in AEDC's PMEL and demonstrated in a transonic wind tunnel (AEDC Propulsion Wind Tunnel 4T).

The two lines selected for experimentation were the 1394.7 nm and 1395.0 nm lines based on the three conditions discussed in Chapter 3 through the use of the absorption model. The first condition considered limiting wavelength range based on available laser(s) and their wavelength ranges. The second condition considered the strength of the line to ensure the selected line would not be too weak or strong. The third and final condition considered spectral line isolation to ensure a neighboring line would not induce error into the fit. The Curve Fitting Tool, utilizing a Voigt line shape model, was then constructed and its operation was verified using the lab absorption cell. Further work was done to refine and increase the accuracy of the algorithm which was then calibrated against a NIST traceable HG.

The LH system was taken to AEDC's PMEL where a calibration was performed using a NIST traceable HG over a X_{H_2O} range from 0.00004 to 0.01255. The raw LH data had approximately a 7% and 12% deviation from the HG data for the 1394.7 nm and 1395.0 nm

lines, respectively. Two trends in the data emerged, the over prediction of the LH at mole fractions below approximately $X_{H_2O}=0.001$ and under prediction of the LH at mole fractions above approximately $X_{H_2O}=0.001$. The cause of the over prediction is unknown, but the under prediction is thought to be caused by error in the baseline fit. Both trends were successfully calibrated out. Additionally, an uncertainty analysis was performed and resulted in a total uncertainty of 11 to 18 PPM for the 1394.7 nm and 1395.0 nm lines respectively.

The last step was to use the calibrated LH system to make humidity measurements in a large scale wind tunnel. This was done in the stilling chamber of AEDC's 4T wind tunnel along with the CMH system and the measured amount of humidity recorded by the LH system fell within approximately 2% of the CMH. This is a very good result showing close correlation to the CMH system which makes the LH technique a very attractive option to measure humidity in 4T. The major remaining unanswered question is how accurate is the CMH when used in this manner and is the LH technique even more accurate? The first question is extremely difficult to answer because there is no exact way to measure the water content in an operational wind tunnel. Thus, when the LH is compared to the CMH and a 2% difference is observed, how does one determine if the CMH system is most accurate? Is it possible that the LH system with 2% error is more accurate? Many scholars and experts in the field would argue that they believe the LH technique is more accurate, but proving that is beyond the scope of this work.

Despite these questions, there are several advantages to the LH system. First, it makes in-situ measurements which prevents errors associated with extracting a sample of the flow and routing it through tubing to the measurement system, unlike the CMH. This also results in the LH system being much simpler since there are no external tubes to troubleshoot for leaks. The

LH system also is more reliable than the CMH system since it does not rely on mirrors that occasionally get dirty and have to go offline to be cleaned.

In conclusion, this work has demonstrated that both systems measure humidity to nearly the same level of accuracy. However, the LH does it using a much simpler and reliable platform. The combination of these attributes make the LH system a very attractive candidate for an operational humidity measurement in AEDC's PWT facilities and possibly beyond.

Future Plans and Recommendations

The next step for this work is to continue moving towards a thoroughly tested operational system by merging the data analysis code with a data acquisition system. Once that task has been successfully completed and tested, the system will be capable of making near real-time measurements on the order of 0.5 seconds. Next, the system must be automated so that once the system is triggered it will record data, analyze the data, return a humidity measurement result and repeat the task at a pre-described frequency without error. Lastly, the system will need to be extensively tested for robustness. In order for the sensor to be solely used during an actual wind tunnel test, it must be robust and dependable; operating for hours on end without failure or error.

REFERENCES

- [1] R. Hanson, "Combustion Gas Measurements Using Tunable Laser Absorption Spectroscopy," in *17th Aerospace Sciences Meeting*, New Orleans, 1979. 79-0086.
- [2] D. S. Baer, V. Nagali, E. R. Furlong and R. K. Hanson, "Scanned- and Fix-Wavelength Absorption Diagnostics for Combustion Measurements Using Multiplexed Diode Lasers," *AIAA Journal*, vol. 34, no. 3, pp. 489-493, 1996.
- [3] V. Nagali, J. Herbon, D. Horning, R. Bates, D. F. Davidson and R. K. Hanson, "Diode-Laser Based Diagnostic to Monitor Water-Vapor in High Pressure Environments," in *37th AIAA Aerospace Sciences Meeting and Exhibit*, Reno, 1999. 99-0942.
- [4] H. Li, A. Farooq, J. Jeffries and R. K. Hanson, "Near-infrared diode laser absorption sensor for rapid measurements of temperature and water vapor in a shock tube," *Applied Physics B - Lasers and Optics*, vol. 89, pp. 407-416, 2007.
- [5] M. E. Newfield, M. P. Loomis, N. K. J. M. Gopaul, A. Ghorbani, T. R. Kowalski and J. A. Cavolowsky, "Optical Fiber Applications of Laser Absorption Diagnostics in Scramjet Combustors," in *32nd Aerospace Sciences Meeting*, Reno, 1994. 94-0386.
- [6] J. T. Liu, G. B. Rieker, J. B. Jeffries, M. R. Gruber, C. D. Carter, T. Mathur and R. K. Hanson, "Near-infrared diode laser absorption diagnostic for temperature and water vapor in a scramjet combustor," *Applied Optics*, vol. 44, no. 31, pp. 6701-6711, 2005.
- [7] J. A. Silver and D. J. Kane, "Diode laser measurements of concentration and temperature in microgravity combustion," *Measurement Science and Technology*, vol. 10, pp. 845-852, 1999.
- [8] S. T. Sanders, D. W. Mattison, T. M. Muruganandam and R. K. Hanson, "Multiplexed Diode-Laser Absorption Sensors for Aeropropulsion Flows," in *39th Aerospace Sciences Meeting & Exhibit*, Reno, 2001. 2001-0412.
- [9] L. S. Chang, J. B. Jeffries and R. K. Hanson, "Mass Flux Sensing via Tunable Diode Laser Absorption of Water Vapor," *AIAA Journal*, vol. 48, no. 11, pp. 2687-2693, 2010.
- [10] L. S. Chang, J. B. Jeffries and R. K. Hanson, "Mass Flux Sensing via Tunable Diode Laser Absorption of Water Vapor," in *48th AIAA Aerospace Sciences Meeting*, Orlando, 2010. 2010-303.
- [11] L. S. Chang, "Development of a Diode Laser Sensor for Measurement of Mass Flux in Supersonic Flow," Ph.D. Dissertation, Mechanical Engineering Dept., Stanford University, Stanford, CA, 2011.

- [12] L. S. Chang, C. L. Strand, J. B. Jeffries and R. K. Hanson, "Supersonic Mass-Flux Measurements via Tunable Diode Laser Absorption and Nonuniform Flow Modeling," *AIAA Journal*, vol. 49, no. 12, pp. 2783-2791, 2011.
- [13] P. R. Wiederhold, "The Principles of Chilled Mirror Hygrometry," *Sensors Magazine*, pp. 46-51, July 2000.
- [14] M. G. Allen, "Diode laser absorption sensors for gas-dynamic and combustion flows," *Measurement Science and Technology*, vol. 9, pp. 545-562, 1998.
- [15] C. N. Patel, "Saturation spectroscopy with a tunable spinflip Raman laser," *Applied Physics Letters*, vol. 25, no. 2, pp. 112-114, 1974.
- [16] B. H. Armstrong, "Spectrum Line Profiles: The Voigt Function," *Journal of Quantum Spectroscopy and Radiative Transfer*, vol. 7, pp. 61-88, 1967.
- [17] J. Humlicek, "Optimized Computation of the Voigt and Complex Probability Functions," *Journal of Quantitative Spectroscopy and Radiative Transfer*, vol. 27, no. 4, pp. 437-444, 1982.
- [18] H. S. Lowry III, "Line Parameter Measurements and Calculations of CO Broadened by H₂O and CO₂ at Elevated Temperatures," *Journal of Quantum Spectroscopy*, vol. 31, no. 6, pp. 575-581, 1984.
- [19] S. Lundqvist, Margolis, J. and J. Reid, "Measurements of pressure-broadening coefficients of NO and O₃ using a computerized tunable diode laser spectrometer," *Applied Optics*, vol. 21, no. 17, pp. 3109-3113, 1982.
- [20] L. Rothman, I. Gordon, Y. Babikov, A. Barbe, D. C. Benner, P. Bernath, M. Birk, L. Bizzocchi, V. Boudon, L. Brown, A. Campargue, K. Chance, E. Cohen, L. Coudert, V. Devi, B. Drouin, A. Fayt, J.-M. Flaud, R. Gamache, J. Harrison, J.-M. Hartmann, C. Hill, J. Hodges, D. Jacquemart, A. Jolly, J. Lamouroux, R. Le Roy, G. Li, D. Long, O. Lyulin, C. Mackie, S. Massie, S. Mikhailenko, H. Muller, O. Naumenko, A. Nikitin, J. Orphal, V. Perevalov, A. Perrin, E. Polovtseva, C. Richard, M. Smith, E. Starikova, K. Sung, S. Tashkun, J. Tennyson, G. Toon, V. Tyuterev and G. Wagner, "The HITRAN2012 molecular spectroscopic database," *Journal of Quantitative Spectroscopy & Radiative Transfer*, vol. 130, pp. 4-50, 2013.
- [21] H. C. Walker Jr. and W. J. Phillips, "High Resolution Tunable Diode Laser Spectroscopy of Methane," Sverdrup Technology, Inc. (Arnold Engineering Development Center Technical Report AEDC-TR-85-37), Arnold AFB, TN, 1986.
- [22] M. P. Arroyo and R. K. Hanson, "Absorption measurements of water-vapor concentration, temperature, and line-shape parameters using a tunable InGaAsP diode laser," *Applied Optics*, vol. 32, no. 30, pp. 6104-6116, 1993.

- [23] M. P. Arroyo, S. Langlois and R. K. Hanson, "Diode-laser absorption technique for simultaneous measurements of multiple gasdynamic parameters in high-speed flows containing water vapor," *Applied Optics*, vol. 33, no. 15, pp. 3296-3306, 1994.
- [24] D. S. Baer, R. K. Hanson, M. E. Newfield and N. K. J. M. Gopaul, "Multi-Species Diode-Laser Sensor System for H₂O and O₂ Measurements," in *18th AIAA Aerospace Ground Testing Conference*, Colorado Springs, 1994. 94-2643.
- [25] R. A. Toth, "Extensive measurements of H₂O line frequencies and strengths: 5750 to 7965 cm⁻¹," *Applied Optics*, vol. 33, no. 21, pp. 4851-4867, 1994.
- [26] S. Langlois, T. P. Birbeck and R. K. Hanson, "Diode Laser Measurements of H₂O Line Intensities and Self-Broadening Coefficients in the 1.4- μ m Region," *Journal of Molecular Spectroscopy*, vol. 163, pp. 27-42, 1994.
- [27] M. Lepere, A. Henry, A. Valentin and C. Camy-Peyret, "Diode-Laser Spectroscopy: Line Profiles of H₂O in the Region of 1.39 μ m," *Journal of Molecular Spectroscopy*, vol. 208, pp. 25-31, 2001.
- [28] M. Troccoli, L. Diehl, D. P. Bour, S. W. Corzine, N. Yu, C. Y. Wang, M. A. Belkin, G. Hofler, R. Lewicki, G. Wysocki, F. K. Tittel and F. Capasso, "High-Performance Quantum Cascade Lasers Grown by Metal-Organic Vapor Phase Epitaxy and Their Applications to Trace Gas Sensing," *Journal of Lightwave Technology*, vol. 26, no. 21, pp. 3534-3555, 2008.
- [29] A. A. Kosterev and F. K. Tittel, "Chemical Sensors Based on Quantum Cascade Lasers," *Journal of Quantum Electronics*, vol. 38, no. 6, pp. 582-591, 2002.
- [30] P. Fuchs, J. Seufert, J. Koeth, J. Semmel, S. Hofling, L. Worschech and A. Forchel, "Widely tunable quantum cascade lasers with coupled cavities for gas detection," *Applied Physics Letters*, vol. 97, no. 18, pp. 181111-181111-3, 2010.
- [31] M. Hubner, S. Welzel, D. Marinov, O. Guaitella, S. Glitsch, A. Rousseau and J. Ropcke, "TRIPLE Q: A three channel quantum cascade laser absorption spectrometer for fast multiple species concentration measurements," *Review of Scientific Instruments*, vol. 82, no. 9, pp. 093102-093102-7, 2011.
- [32] X. Chao, J. B. Jeffries and R. K. Hanson, "In situ absorption sensor for NO in combustion gases with a 5.2 μ m quantum-cascade laser," *Proceedings of the Combustion Institute*, vol. 33, no. 1, pp. 725-733, 2011.
- [33] I. A. Schultz, C. S. Goldenstein, R. M. Spearrin, J. B. Jeffries, R. K. Hanson, R. D. Rockwell and C. P. Goyne, "Multispecies Midinfrared Absorption Measurements in a Hydrocarbon-Fueled Scramjet Combustor," *Journal of Propulsion and Power*, vol. 30, no. 6, pp. 1595-1604, 2014.

- [34] R. K. Hanson, R. M. Spearrin and C. S. Goldenstein, "1.10 Boltzmann Distribution," in *Spectroscopy and Optical Diagnostics for Gases*, New York, Springer International Publishing, 2016, p. 8.
- [35] W. Demtroder, "2.2 Thermal Radiation and Plank's Law," in *Laser Spectroscopy Volume 1 Basic Principles*, Berlin Heidelberg, Springer-Verlag, 2008, pp. 9-10.
- [36] J. Buldyreva, N. Lavrentieva and V. Starikov, "1.2 Principle line-broadening mechanisms and model profiles," in *Collisional Line Broadening and Shifting of Atmospheric Gases*, London, Imperial College Press, 2011, pp. 3-7.
- [37] N. Galyen and D. Plemmons, "Optical Mass Flux Sensor," in *27th AIAA Aerodynamic Measurement Technology and Ground Testing Conference*, Chicago, 2010. 2010-4910.
- [38] A. P. Thorne, "10.3 Doppler Broadening," in *Spectrophysics Second Edition*, London, Chapman and Hall Ltd, 1974, p. 262.
- [39] M. Kuntz, "A New Implementation of the Humlicek Algorithm for the Calculation of the Voigt Profile Function," *Journal of Quantitative Spectroscopy and Radiative Transfer*, vol. 57, no. 6, pp. 819-824, 1997.
- [40] K. L. Letchworth and D. C. Benner, "Rapid and accurate calculation of the Voigt function," *Journal of Quantitative Spectroscopy and Radiative Transfer*, vol. 107, pp. 173-192, 2007.
- [41] S. M. Abrarov, B. M. Quine and R. K. Jagpal, "Rapidly convergent series for high-accuracy calculation of the Voigt function," *Journal of Quantitative Spectroscopy and Radiative Transfer*, vol. 111, pp. 372-375, 2010.
- [42] A. Farooq, J. B. Jeffries and R. K. Hanson, "In situ combustion measurements of H₂O and temperature near 2.5 μ m using tunable diode laser absorption," *Measurement Science and Technology*, vol. 19, pp. 1-11, 2008.